

Journal of Thermal Stresses



ISSN: (Print) (Online) Journal homepage: https://www.tandfonline.com/loi/uths20

Stress waves in laser-material interaction: From atomistic understanding to nanoscale characterization

Shen Xu & Xinwei Wang

To cite this article: Shen Xu & Xinwei Wang (2023) Stress waves in laser-material interaction: From atomistic understanding to nanoscale characterization, Journal of Thermal Stresses, 46:6, 464-491, DOI: <u>10.1080/01495739.2023.2204126</u>

To link to this article: https://doi.org/10.1080/01495739.2023.2204126







Stress waves in laser-material interaction: From atomistic understanding to nanoscale characterization

Shen Xu^a and Xinwei Wang^b

^aSchool of Mechanical and Automotive Engineering, Mechanical Industrial Key Laboratory of Boiler Low-Carbon Technology, Shanghai University of Engineering Science, Shanghai, PR China; ^bDepartment of Mechanical Engineering, Iowa State University, Ames, Iowa, USA

ABSTRACT

During pulsed laser-assisted manufacturing, the extremely high-temperature gradient in space will lead to very high-stress waves that play a critical role in structuring. Both shear and normal stress waves emerge in space. This work provides a review and perspective based on our past work spanning theoretical analysis, 1D molecular dynamics (MD) modeling, 3D MD modeling, and experimental characterization. Discussions are given on the non-Fourier effect during ultrafast laser-material interaction, stress-induced structural defects in recrystallization, and ablation confinement by ambient gas and nanotip during nanotip-assisted near-field nanomanufacturing. The presence of stress waves in space could cause permanent and temporary damages, and these damages are more caused by the shear stresses than the normal ones where the compressive component usually is much stronger than the tensile part. Due to the fact of very fast stress waves propagation and slow cooling and solidification, it is very challenging to conduct MD modeling of the entire domain even using stage-of-the-art parallel computation. Hybrid modeling that combines MD and macroscale modelings provides a better choice to tackle this problem. Time-resolved ultrafast temperature and stress characterization are still highly needed to provide deep physics understanding of laser-material interaction toward process control and optimization.

ARTICLE HISTORY

Received 6 March 2023 Accepted 21 March 2023

KEYWORDS

Experimental probing; molecular dynamics simulation; pulsed laser heating; stress wave; structural evolution; thermal transport

1. Introduction

To date, lasers have been widely used in material processing, synthesis, and manufacturing. Examples include pulsed laser deposition, laser shock peening, laser welding, 3D additive manufacturing, and 3D subtractive manufacturing [1–5]. The involved pulsed laser-material interaction spans time domains of ms, μ s, down to fs time scale. Under intense laser irradiation, the target material will experience extremely fast heating, melting, vaporization, and phase explosion with an extremely high-temperature gradient in the material. This very large temperature gradient will form extremely high-stress waves that can propagate in the material, and whose existence will cause strong structure alteration, destruction, and affect the subsequent solidification and crystal-lization processes. Because of the intensive physical processes, experimental, theoretical, and numerical modeling studies of laser-material interaction and the stress waves become very challenging. Despite extensive work reported in the past, tremendous research is still being conducted worldwide in this area. This article is not intended to provide an extensive review of stress waves



in laser-material interaction, which is truly a broad topic. Rather we focus on the research we have conducted that covers theoretical work, numerical modeling (mostly molecular dynamics [MD] simulation), and experimental characterization of stress waves during laser-material interaction, and elaborate on our perspectives in this area.

2. Stress waves in pulsed laser-material interaction: 1D frame

2.1. 1D frame consideration under simplified physics

Under intense pulsed laser irradiation, the target material will experience very fast temperature rise, melting, vaporization, and phase explosion in a 3D domain [6-8]. Also, plasma will be generated in the ablated-out plume. All these processes are conjugated and complicated, and will combine together to influence the temperature evolution and distribution in the target, which in turn strongly affect stress waves formation and propagation. Precise analytical analysis and highfidelity modeling are extremely difficult to do. A good way to understand the involved physical processes is to rather focus on some effects with significantly simplified factors. Under the frame of neglecting phase change and temperature effect on properties, the 1D heat transfer and displacement generation in the target can be described by the below equations: [9]

$$\rho c_p \frac{\partial T}{\partial t} = \frac{\partial q''}{\partial x} + \beta I(t) e^{-\beta x},\tag{1}$$

$$\rho \frac{\partial^2 u}{\partial t^2} = \left(B + \frac{4}{3} G \right) \frac{\partial^2 u}{\partial x^2} - B \beta_T \frac{\partial T}{\partial x}. \tag{2}$$

Here ρ , c_p , B, G, and β_T are the density, specific heat, bulk and shear moduli of elasticity, and thermal expansion coefficient of the target. T and u are temperature and displacement in the x direction, and β is the laser beam absorption coefficient as $\beta = 1/\tau_e$ (τ_e the laser beam absorption depth). I is the laser intensity that varies with time. Under the validity of Fourier's law of heat conduction, we will have $q'' = -k\partial T/\partial x$ with k as the thermal conductivity of the target. Under very fast laser heating, e.g., the laser pulse width is comparable to or shorter than the energy carriers thermal relaxation time, or called mean free time τ, this relation has to be modified as (1 + $\tau \partial/\partial t)q'' = -k\partial T/\partial x$ to account for the time delay between heat flux and temperature gradient. This effect is termed "non-Fourier effect". Such consideration will lead to the second sound wave, which is usually observed under reduced temperatures where the energy carriers experience significantly reduced phonon scattering and will have a much longer mean free time. Recent work has reported second sound wave over 200 K in graphite, whose very high thermal conductivity and low phonon scattering enabled this observation [10]. The displacement and temperature of the target are similar to the displacement and kinetic energy of a harmonic oscillator, whose potential and potential energies exchange with each other continuously. Therefore, in fact the temperature of the target could be varied by the strong local stress (related to potential energy). Under such frame, the right side of Eq. (1) will have an extra term as $-B\beta_T T_0 \cdot \partial^2 u/\partial x \partial t$ where T_0 is the equilibrium temperature [11].

For most cases, laser beam absorption in a material is by free electrons, who will experience the temperature rise first, then transfer the energy to lattice (or termed phonons). With temperature rise and gradient in space in lattice, a displacement will occur and a normal stress wave will form. Note for 1D heating case, no shear stress waves will emerge since the temperature gradient only exists in one direction. This holds true for both analytical solution and modeling discussed in the next section. Usually, the energy transfer between electrons and lattice is very fast, can be thought as instantaneous. However, when the laser pulse is very short, e.g., less than 1 ps, such energy transfer is relatively slow compared with the heating process. It will cause strong thermal nonequilibrium between electrons and phonons, and result in delayed lattice heating and stress formation. To account for this situation, the two-step heating has to be considered, which treats the temperatures of electrons (T_e) and phonons/lattice (T_l) separately [12]:

$$C_e \frac{\partial T_e}{\partial t} = \frac{\partial}{\partial x} \left(k_e \frac{\partial T_e}{\partial x} \right) - G_{el}(T_e - T_l) + \beta I(t) e^{-\beta x}, \tag{3}$$

$$C_{l}\frac{\partial T_{l}}{\partial t} = \frac{\partial}{\partial x} \left(k_{l} \frac{\partial T_{l}}{\partial x} \right) + G_{el} (T_{e} - T_{l}) - B \beta_{T} T_{0} \frac{\partial^{2} u}{\partial x \partial t}. \tag{4}$$

Here, C_e and C_l are the volumetric specific heat of electrons and lattice. Usually, it is true that $C_e \ll C_l$. Note for metals the electron thermal conductivity k_e usually is much larger than that of lattice: k_l , therefore the heat conduction in lattice can be neglected in metals. In alloys, the elements which are added as alloying agents will cause extra electron scattering and reduce the electron thermal conductivity. But under laser irradiation, the heating mechanism is the same as metals: electrons absorb photon energy first, then transfer it to lattice. So the above equations are applicable to alloys. However, this is not true for many materials like semiconductors or materials experiencing nonlinear laser beam absorption for electron excitation. Under these situations, both electron and lattice heat conductions are important. The term $G_{el}(T_e - T_l)$ in the above equations represents the energy coupling between electrons and lattice with an energy coupling coefficient G_e . For this situation, T_l will need to be used in Eq. (2) for displacement calculations. It needs to be pointed out that under intense laser irradiation, the very high-temperature rise will reduce the target's thermal conductivity significantly, so its energy carrier's mean free time τ . This will make the non-Fourier effect much less important, or become negligible. When the temperature and displacement are solved, the local stress can be calculated as [12]

$$\sigma = \left(B + \frac{4}{3}G\right)\frac{\partial u}{\partial x} - B\beta_T(T - T_0). \tag{5}$$

Up to date, tremendous research has been reported on temperature and stress waves during pulsed laser absorption with consideration of the non-Fourier effect or two-step heat transfer [9]. It needs to be pointed out that the energy carrier mean free time sometimes is overstated in a lot of work, making the non-Fourier effect unrealistically strong. The energy carrier mean free time should be rigorously evaluated from the equation $k = 1/3 \cdot \rho c_p v^2 \tau$ under the single relaxation time frame, where ν is the energy carrier velocity. For 2D and 1D materials, the coefficient "1/3" in this equation will become "1/2" and "1".

Figure 1 shows the stress wave in a gold target irradiated by a picosecond laser pulse (50 ps full width at half maximum: FWHM, 800 nm wavelength) to show how the two-step heat transfer consideration affects the stress wave formation and propagation. Note all the laser pulse widths

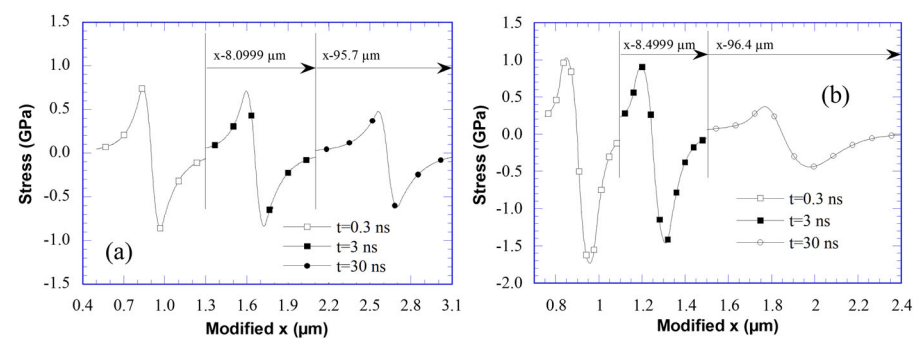


Figure 1. Stress wave in a gold target irradiated by a ps laser pulse: (a) with consideration of two-step heat transfer; (b) without consideration of two-step heat transfer. The *x* coordinate's origin is at the target surface. Reproduced from Wang and Xu [12] with permission from Taylor & Francis Ltd, copyright 2002.

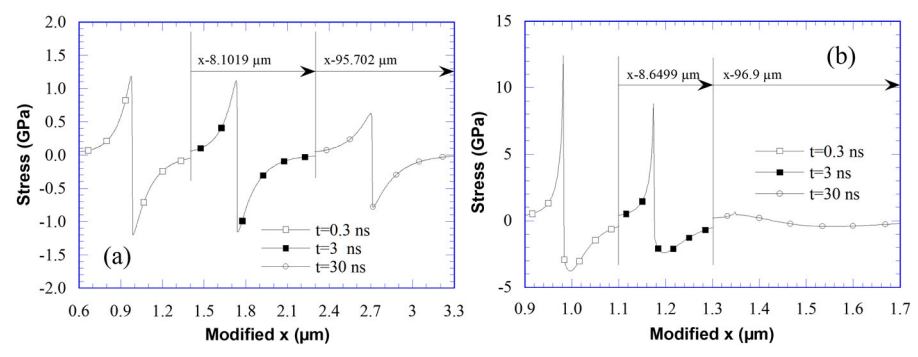


Figure 2. Stress wave in a gold target irradiated by a fs laser pulse: (a) with consideration of two-step heat transfer; (b) without consideration of two-step heat transfer. Reproduced from Wang and Xu [12] with permission from Taylor & Francis Ltd, copyright 2002.

mentioned in this article are FWHM. It is obvious that with consideration of the two-step heat transfer, the stress wave is more stretched in space and experiences slower attenuation during propagation. Such effect is more evident for the fs laser pulse case (200 fs pulse width and 800 nm wavelength) shown in Figure 2. In fact, for fs laser irradiation, the stress wave is in the GHz range although the laser heating time is very fast. This slow response of the stress wave is caused by the fact that the heat conduction in the target determines the temperature gradient, which in turn determines the stress wave formation. The heat conduction, in contrast to the fast laser heating, is a slower process, and is in the order of ns for surface temperature relaxation.

2.2. Molecular dynamics modeling of stress wave under pulsed laser irradiation in vacuum

MD simulation, which tracks the movement of individual atoms within a system, is a powerful tool to investigate large-spectrum physical processes under extreme conditions, such as the extremely fast laser-material interaction [13]. It could capture the very complicated and conjugated physical processes involved in pulsed laser-material interaction. However, it takes quite a large domain to observe and study the behavior of stress waves generation and propagation in space. For instance, for a stress wave with a propagation speed of $3000 \,\mathrm{m/s}$, for a very short time of 5 ns, it will need 15 μ m length to observe its behaviors. Even using parallel computation, such size is still very challenging to model.

To enable large size and long-time stress waves behavior study using MD simulation, generally speaking, it will be more feasible to model a system of simple potential between atoms (e.g., Lennar-Jones [LJ] potential) under a quasi-3D frame: long in one direction (laser incident direction), reasonable size in the second dimension, and very small length in the third dimension [14]. This is critical to observing the intensive phase change, multi-phase flow, and detailed physics of stress waves formation and propagation. Even though the materials are less realistic, but the general conclusions hold true for a broad range of materials. Figure 3 shows the 1D stress wave propagation behavior along with the temperature distribution within an argon crystal (50 K) under ps laser beam irradiation. The laser pulse has a width of 5 ps and absorption depth of 2.5 nm. The stress wave behavior reflects the dynamic process of formation, propagation, and reflection at the backside of the target (x = 50 nm). More interestingly, a temperature wave accompanies the stress wave, perfectly reflects the potential, and kinetic energy exchange: when the material is compressed, its atomic potential energy increases and the local temperature/kinetic energy decreases, and vice versa. Note the laser-material interaction is a very complicated process, and involves intensive phase change, particle formation, and solidification. As our focus of this article is the stress in the solid, readers may refer to other work for the above behaviors [15]. The stress wave behaviors in Figure 3 are for a case that the target is placed in a vacuum, and no

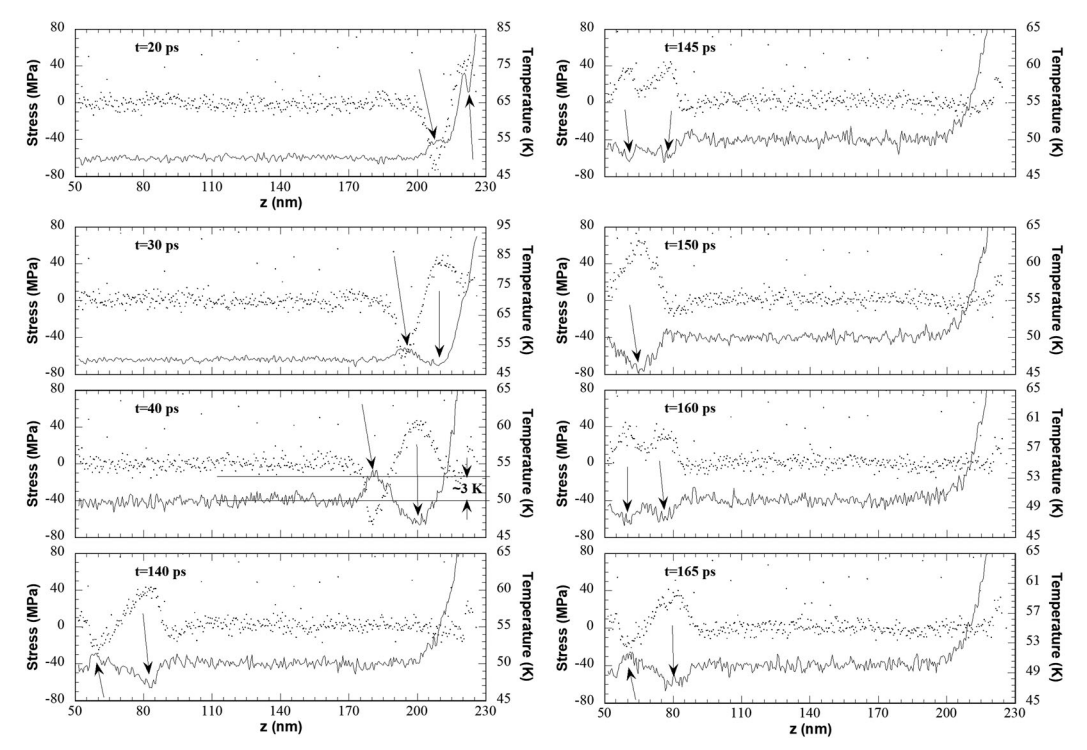


Figure 3. Stress wave formation and propagation, along with the temperature field, in argon under ps laser irradiation. Solid line: temperature, dots: stress. Reproduced from Wang and Xu [16] with permission from Elsevier, copyright 2003.

ambient gas is present. Therefore, the material ablation sees no impedance from the ambience. However, when an ambient gas is present, a strong shock wave will form, which significantly affects the ablation process, so as the shock wave in the solid.

2.3. Stress wave behaviors under the presence of ambient gas

Presence of an ambient gas during pulsed laser-material interaction will have strong effect on the ablation behavior due to the confinement by the shock wave [13,17-21]. Also, this confinement will affect the recoil pressure in the solid part, subsequently affecting the stress wave behaviors. Additionally, the shock wave will affect the molten part's behavior as well as the ablation process. Figure 4 shows the shock wave confinement effect on the ablation behavior. A model material of argon is used in the MD modeling. It is observed that when the absorption depth is large, the ablation is weak due to the lower temperature rise, and bubbles could form and then collapse due to confinement by the shock wave. Also, the shock wave front is clearly observed to have a higher density. This is also clearly shown in the atom number density evolution in Figure 5a,b. The same physics also holds true for the stress wave in the solid target part: the local stress wave will alter the atom number density, which can be used to clearly indicate the stress wave propagation. This is shown in Figure 5c,d. Also, Figure 5d shows the re-deposition process of ablated materials due to shock wave confinement. Figure 6 shows the comparison of the stress waves within the target when ambient gas is and not present. Overall, the shock wave in the ambient gas has quite weak effect on the stress wave in the solid. This is because the early stage of ablation and heating determines the stress wave formation while at these instances the ambient gas effect is relatively weak.

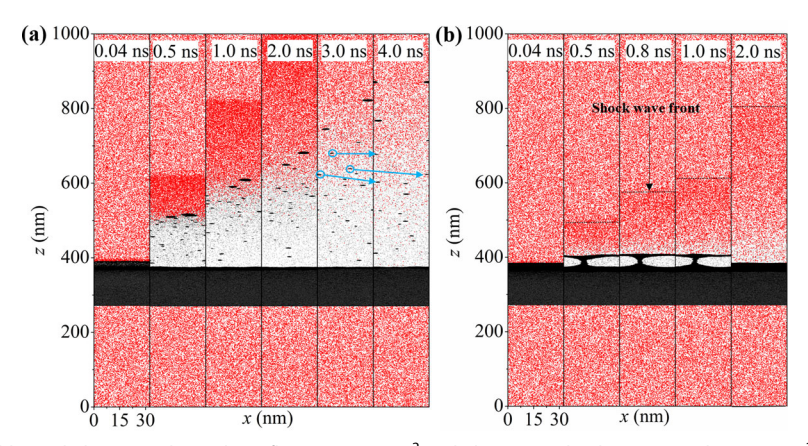


Figure 4. The ablation behavior under (a) laser fluence E=3 J/m² and absorption depth $\tau=5$ nm; (b) E=3 J/m² and $\tau=15$ nm. Red dots represent the ambient gas and black ones are for the target material. Reproduced from Li et al. [22] with permission from Springer Nature, copyright 2013.

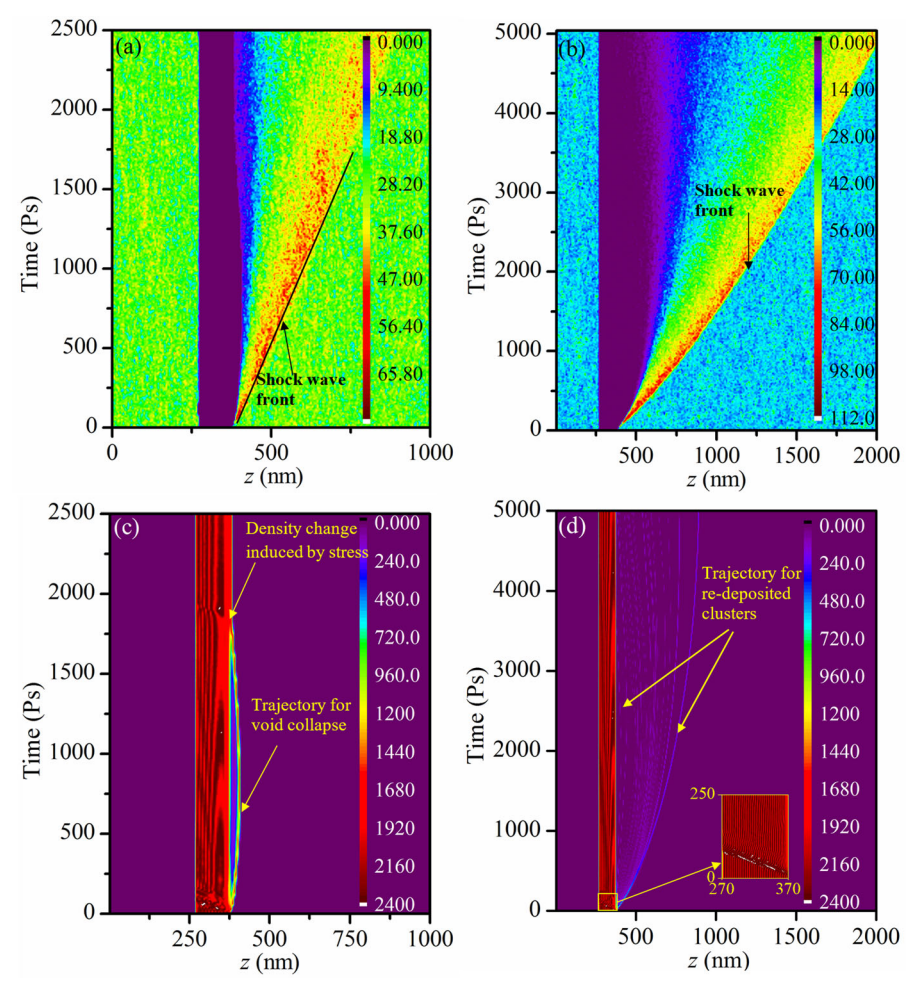


Figure 5. The atom number density evolution of the ambient gas for (a) E=3 J/m², $\tau=15$ nm and (b) E=3 J/m², $\tau=5$ nm. The atom number density evolution of the target for (c) E=3 J/m², $\tau=15$ nm and (d) E=3 J/m², $\tau=5$ nm. The stress wave in the target is clearly visible: deformed twisted lines in the number density contours show the local density change by the stress wave. The inset in Figure d shows stress wave propagation. Reproduced from Li et al. [22] with permission from Springer Nature, copyright 2013.

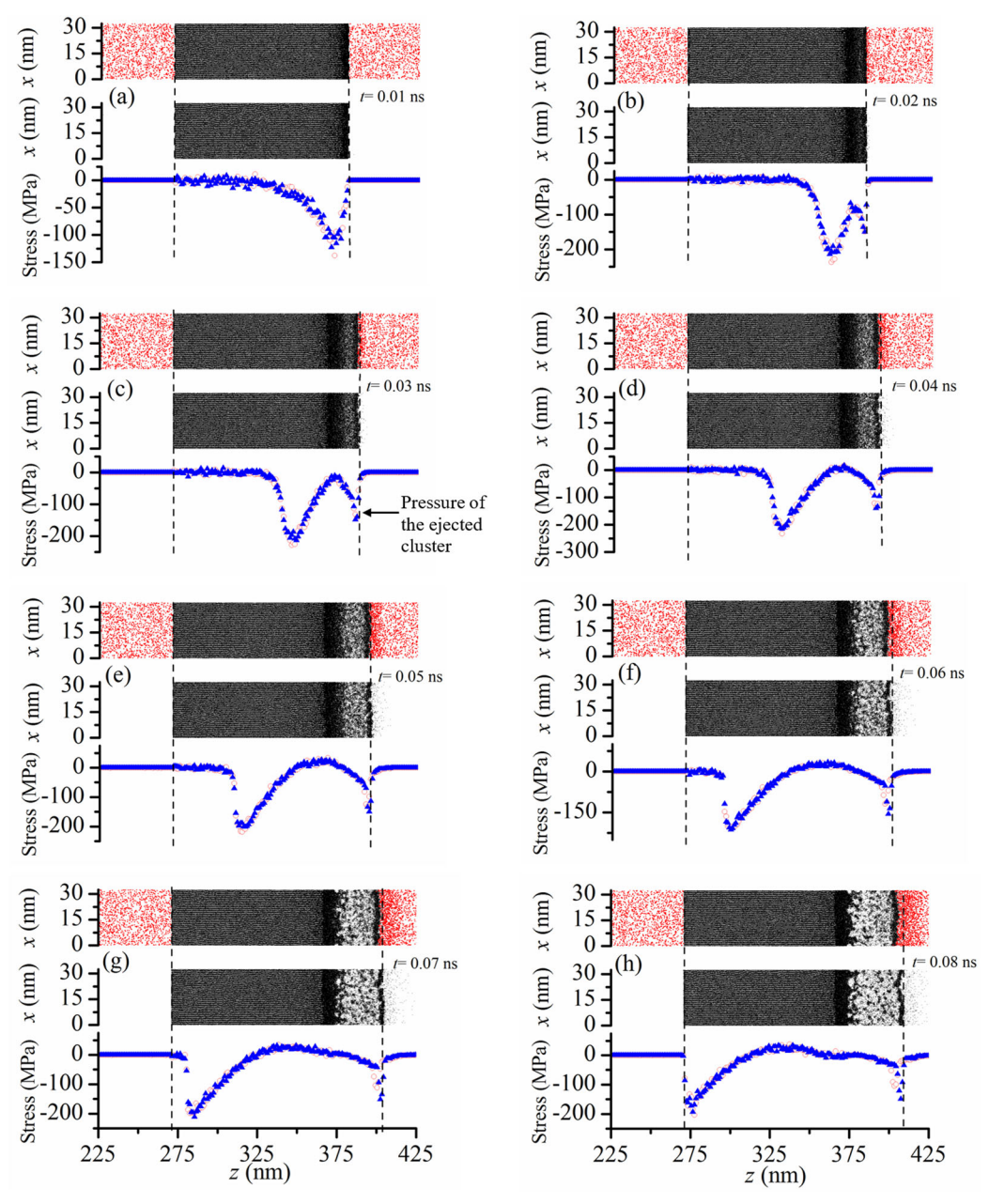


Figure 6. Comparison of stress wave formation and propagation in the target with and without ambient gas. The blue symbol is for case without ambient gas, and the red one is for the case with ambient gas. Reproduced from Li et al. [22] with permission from Springer Nature, copyright 2013.

2.4. Stress wave effect on relatively cold material sintering

As seen in the above review, the stress wave generated by pulsed laser heating has a quite high compressive part. This part, if strong enough, could cause permanent structural change and make the material harder. This is the principle of the widely studied laser shock wave peening and surface hardening [23]. Also, such very strong compressive stress can be used for relatively cold

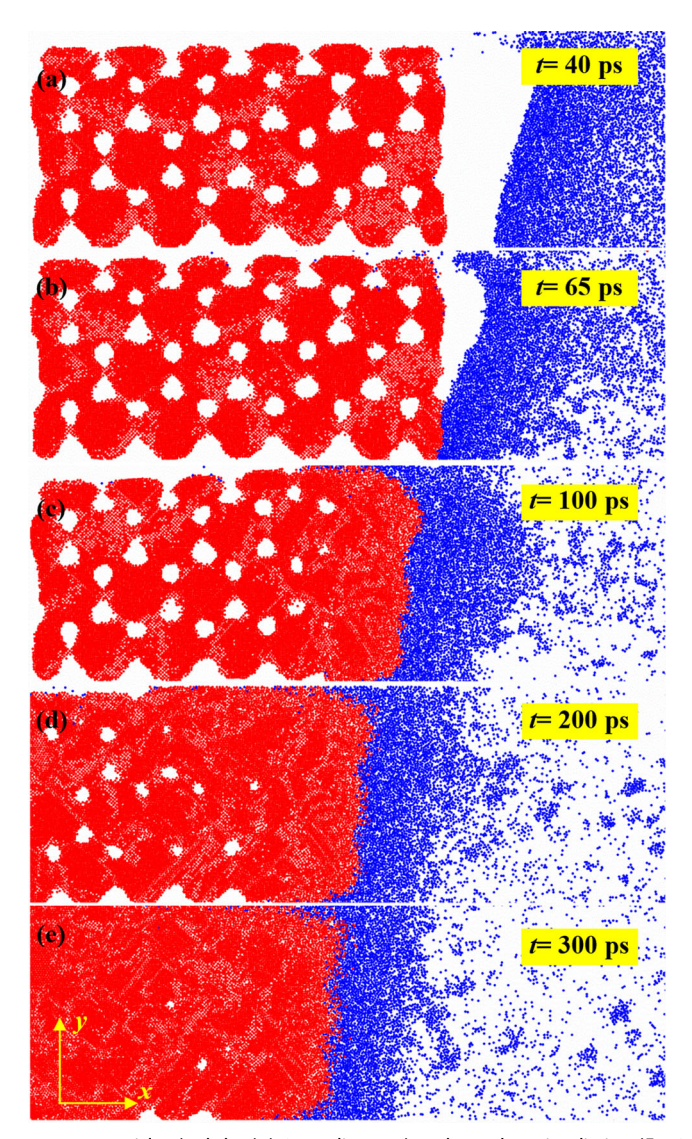


Figure 7. Evolution of argon nanoparticles (red dots) (10 nm diameter) under ps laser irradiation ($E = 2.7 \text{ mJ/cm}^2$, 11.5 ps pulse width). A sacrificial layer of 13.8 nm is added on top of the nanoparticle (the blue dots). Reproduced from Li et al. [24] with permission from Elsevier, copyright 2014.

nanoparticle sintering to form needed solid structures [24]. Such process has been demonstrated in our MD modeling of argon nanoparticles under ps laser irradiation. Figure 7 shows a process studied in our work that argon nanoparticles are compressed and sintered under the compressive stress [24]. In the physical domain, a sacrificial layer is placed at the top, which is used to absorb the laser beam (11.5 ps pulse width), support ablation, and generate a compressive stress that will propagate toward inside to compress the nanoparticles. Argon atoms are studied instead of realistic materials (e.g., Cu, Si and so on), so the modeling is rather to uncover the involved physics. At 300 ps, the material is compressed to a very high density by the compressive stress wave. Such compression effect is strongly related to the particle size and laser pulse fluence. Figure 8 shows the material structure after 1.04 ns compressing for different particle sizes and laser fluence. Generally speaking, when the particle size is larger, a higher laser fluence is needed to compress

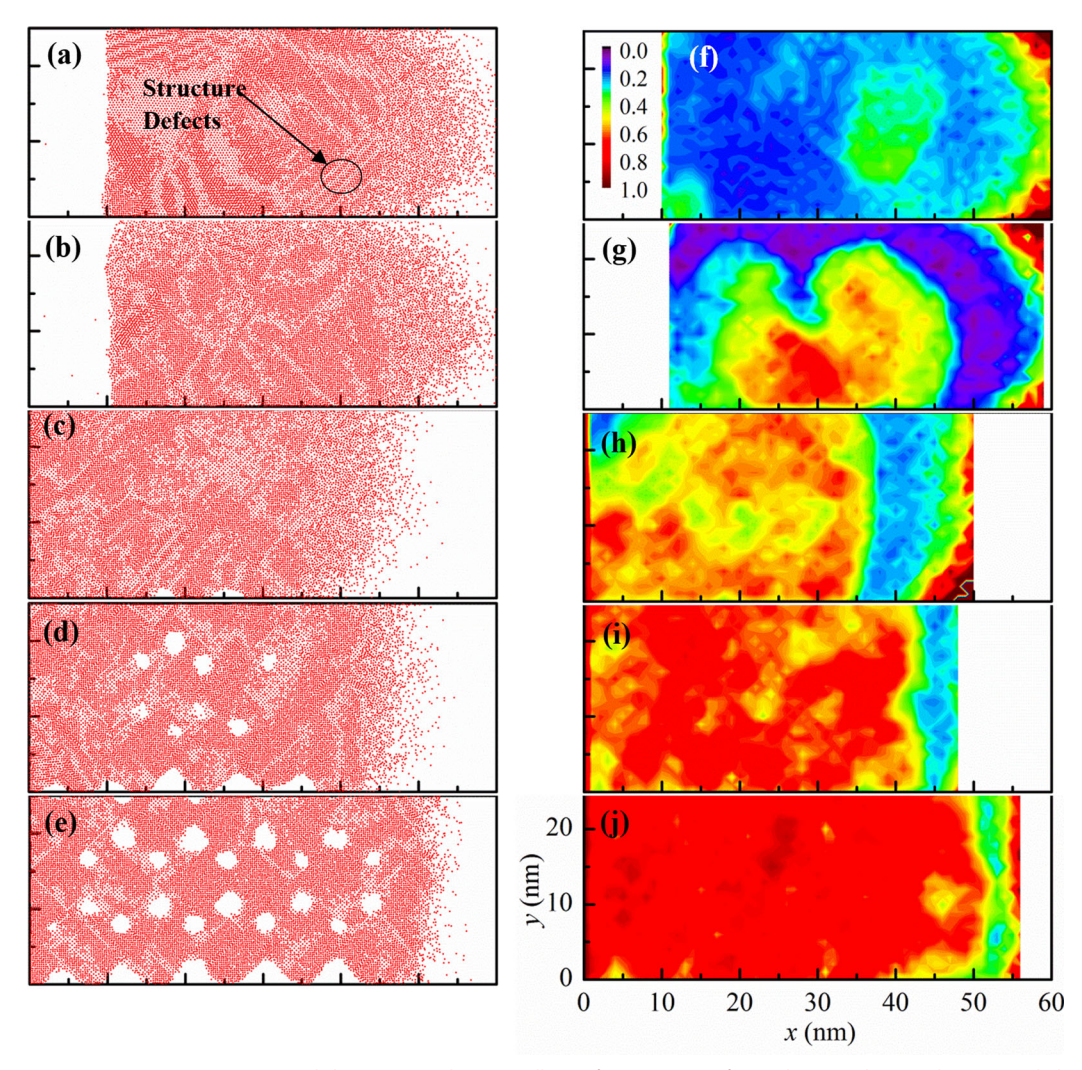


Figure 8. Atomic structure (a-e) and the corresponding crystallinity (f-j) at 1.04 ns after ps laser irradiation. This is intended to demonstrate the effect of laser fluence (E) and particle size (D). The cases are for (a) and (f): D = 5 nm, E = 2.7 mJ/cm²; (b) and (g): D = 8 nm, $E = 2.7 \text{ mJ/cm}^2$; (c) and (h): D = 10 nm, $E = 2.7 \text{ mJ/cm}^2$; (d) and (i): D = 10 nm, $E = 2.0 \text{ mJ/cm}^2$; (e) and (j): D = 10 nm, $E = 1.5 \text{ mJ/cm}^2$. Reproduced from Li et al. [24] with permission from Elsevier, copyright 2014.

and consolidate the particles. During structural evolution, the crystallinity knowledge is critical to in-depth understanding of the whole physics. A crystallinity function is constructed as [24]:

$$\phi(r_{i,x}) = \frac{1}{N} \left| \sum_{i} e^{j2\pi(2r_{i,x}/\lambda)} \right|,\tag{6}$$

where $r_{i,x}$ is the x coordinate of atom i and λ is the light wavelength assumed for structure probing (like x-ray diffraction). Here λ takes a value of $a = 5.414 \,\text{Å}$ (the lattice constant of the material). This function in fact studies the diffraction of light beams when they irradiate atoms and are reflected back in the x direction. The ϕ value clearly shows different levels of crystallinity after stress wave compressing and consolidation.

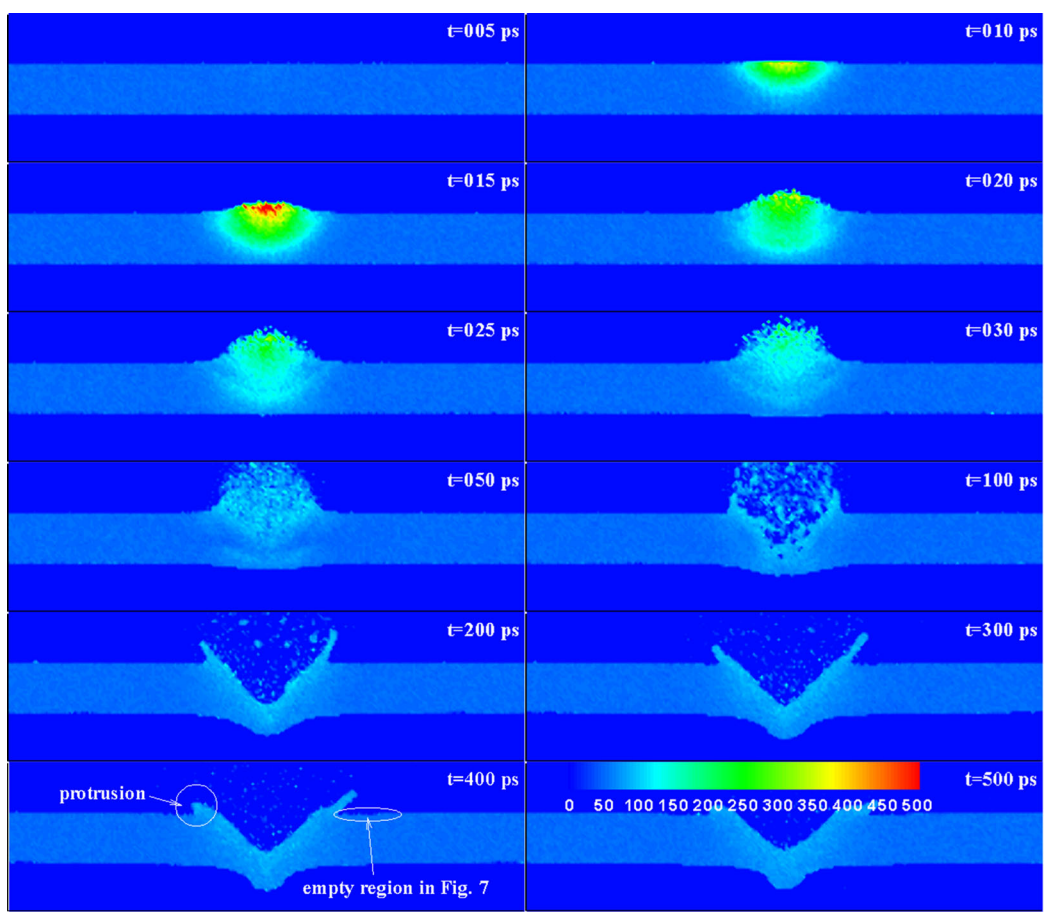


Figure 9. The contour of temperature distribution in an x-z plane centered at y=174.53 nm. Reproduced from Wang [25] with permission from IOP Publishing, copyright 2005.

3. Stress waves in laser-material interaction: 3D frame

3.1. Dynamic behaviors of stress waves under surface laser ablation

Modeling under 1D frame can well illustrate some important physical phenomena and mechanisms along the thickness direction. However, in practical laser-assisted micro/nano-manufacturing, thermal behaviors, and the generation and propagation of stress waves in the lateral directions are also very important. The very large domain size requirement for such 3D modeling has limited the research progress in this area. To overcome this challenge, the LJ potential provides the great advantage to simulate a model material without losing generality of the physical conclusion. Given that stress waves propagate fast in solids, we [25] built a large computational domain consisting of >200 million atoms and employed a large-scale parallel MD program to investigate the thermal and mechanical behavior in the process under the scenario of laser-assisted scanning tunneling microscope (STM) manufacturing. An argon crystal at 50 K with dimensions of 350.83 nm × 350.83 nm \times 32.48 nm $(x \times y \times z)$ was used as the target. A ps laser pulse is used as the heating source. It is focused by a STM tip to a small spot of several nanometer diameter on the target surface (in the x-y plane). The laser pulse energy is 1.6×10^{-14} J. In the above-discussed 1D modeling, with an emphasis on the physical behavior in the thickness direction, the laser intensity is usually assumed uniform in the irradiating area. During 3D modeling, the distribution of the enhanced optical field under the STM tip is considered in space and time domains.

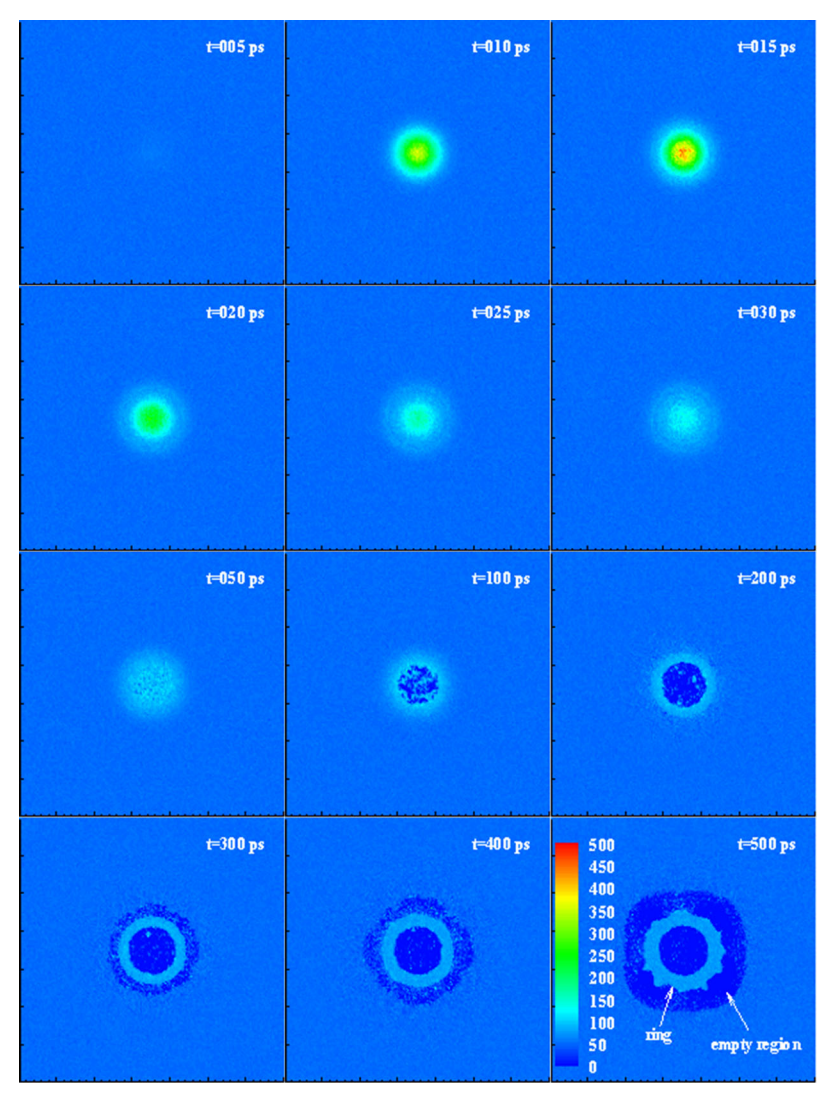


Figure 10. The contour of temperature in an x-y plane centered at z = 245.34 nm. Reproduced from Wang [25] with permission from IOP Publishing, copyright 2005.

Figures 9 and 10 show the temperature evolution from a cross-sectional view (x-z plane) close to the center of the irradiated area and a top view (x-y) plane) at the top surface of the target, respectively. The laser pulse begins heating the target at 5 ps and ends at 15 ps. During pulse heating, the heated region absorbs a large amount of the incident energy and its surface temperature quickly rises to 500 K. Substantial thermal expansion occurs due to the elevated temperature in the heated region and raises a strong compressive thermal stress because of large temperature gradient. Figure 11 shows the stress pattern evolution of the normal stress wave in the x-y plane. After the pulse ends, the surface of the heated region begins to expand and explode. Part of the heat leaves with the ejected argon atoms and the rest is conducted away in the solid to the region of lower temperature. The compressive thermal stress wave propagates outbound from the heated region along with heat conduction. A weak tensile stress in the order of 50 MPa comes after. The stress wave distribution gradually changes from a circular shape to a square shape after 25 ps. A possible reason is that the argon crystal has two different stress wave speeds in [100] and [110] directions. The stress wave toward four angles, the [110] direction, moves a little faster than those

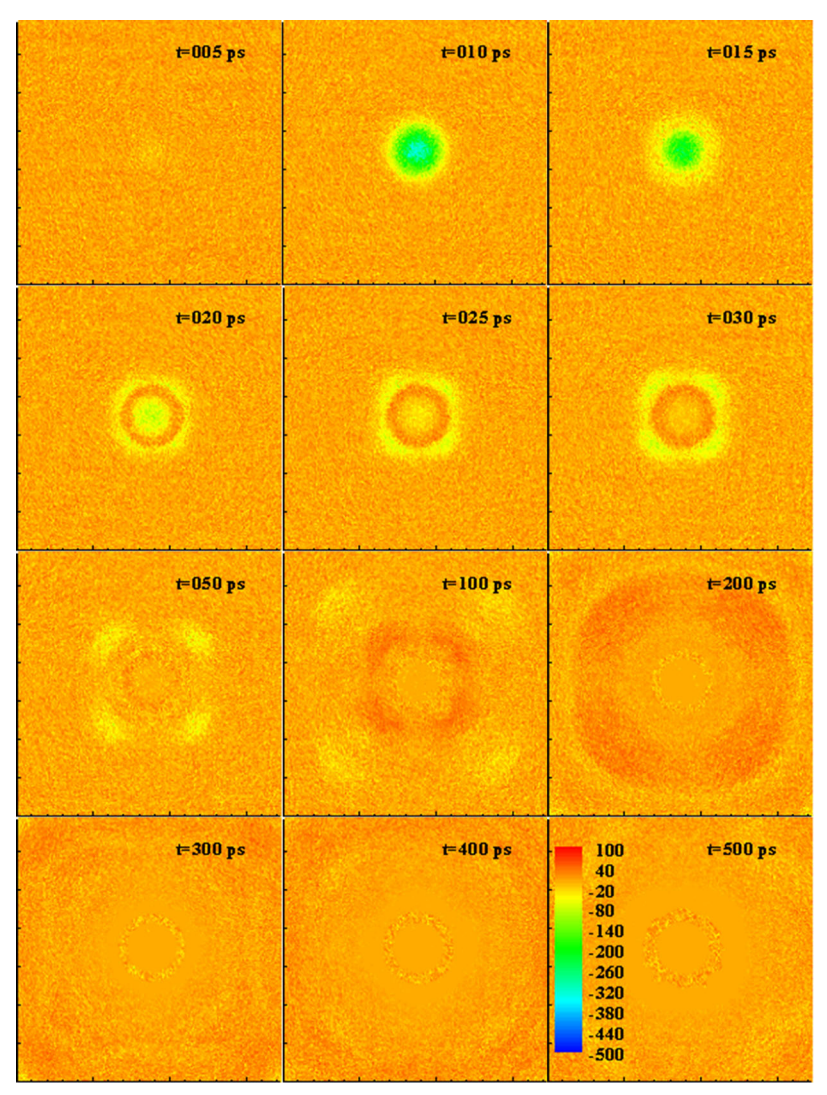


Figure 11. The contour of normal stress σ_{rr} (MPa) in an x–y plane centered at z= 245.34 nm. Reproduced from Wang [25] with permission from IOP Publishing, copyright 2005.

along the x and y directions. From 300 ps and after, the pattern of the stress wave is more complicated because of the periodical boundary condition in both x and y directions. It means when reaching the x and y boundaries, the stress wave will reenter the crystal from the opposite boundary. The reflected stress wave interacts with the forward one and makes the stress wave pattern complicated. Thus, the boundary has significant effects on the stress wave propagation in this modeling, though it is not true in the real laser-assisted STM nano-manufacturing. Compared with the normal stress discussed above, the shear stress $\sigma_{r\theta}$ propagation in the x-y plane is less obvious as shown in Figure 12. It is only visible at the end of the laser pulse (20 ps) with a magnitude of about 30 MPa because the circumferential temperature gradient is small in this symmetric system.

In the z direction, since lots of atoms are ablated away from the surface during the phase explosion, the compressive normal stress moves toward the bottom of the target and is then reflected as a tensile stress at the boundary in the z direction, very much like the 1D reflection

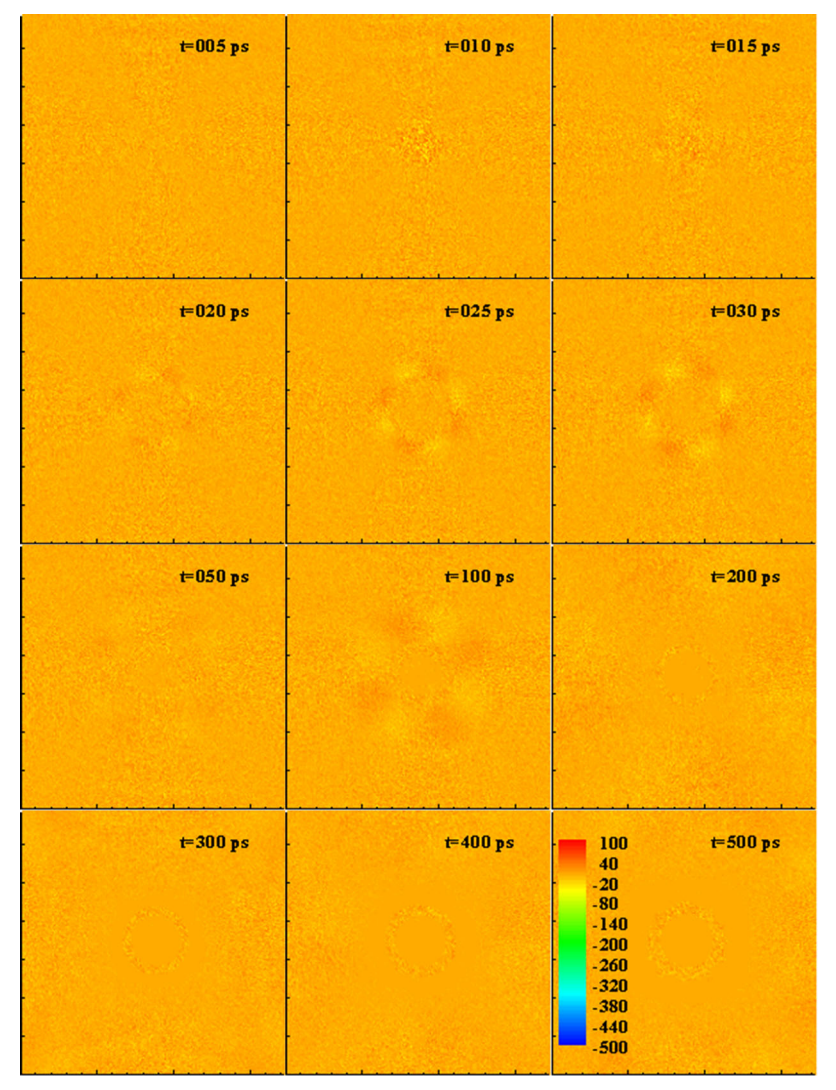


Figure 12. The contour of shear stress $\sigma_{r\theta}$ (MPa) in an x-y plane centered at z = 245.34 nm. Reproduced from Wang [25] with permission from IOP Publishing, copyright 2005.

behaviors shown in Figure 3. Both the tensile stress and shear stress cause structural damage in the crystal beneath the surface. Figures 13 and 14 illustrate atom position at the moment of 100 ps and 200 ps, respectively, and reveal the detailed structure in the crystal. The damages in the x-z plane in Figure 13, the dark lines, representing sub-surface damages, appear at the bottom of the target. They align along 45° with respect to the z direction due to occurrence of the maximum shear stress in this direction. In the x-y plane in Figure 14, the damages also follow 45° with respect to both x and y directions. One possible reason accounting for this phenomenon is the geometrical structure of the target. Shear stress in the 45° direction is normal to the connection between the closest atomic pairs, meaning that the shear stress can easily shift atoms in space. This prompts a very important conclusion that in laser-material interaction, it is the shear stress rather than the normal stresses that tends to cause the highest level structural damage.

Solidification and epitaxial regrowth after laser irradiation in the target is important for final surface nanostructures. Different from the ultrafast laser pulse heating (tens of picoseconds or shorter), solidification is a relatively slow process driven by heat conduction inside the target.

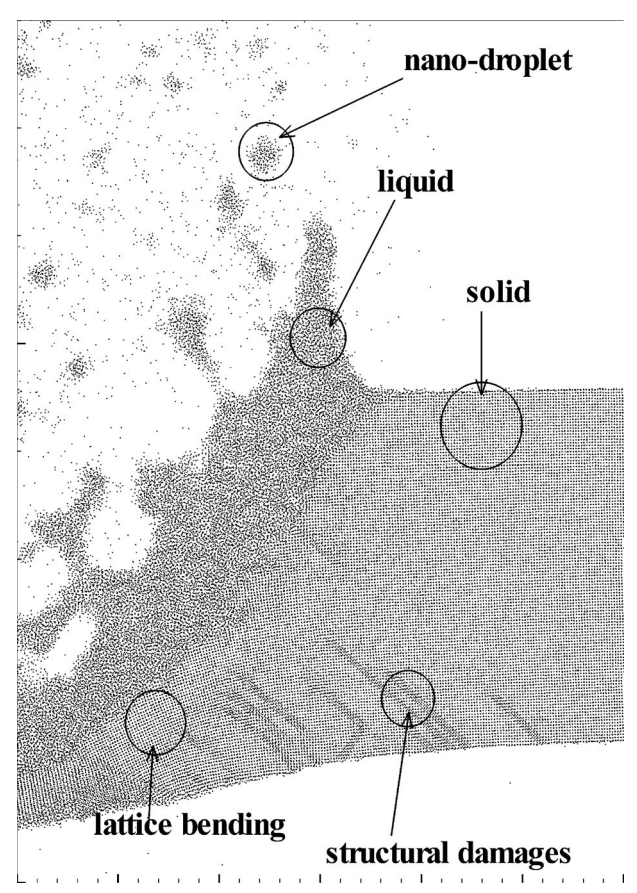


Figure 13. Detailed atomic positions at t = 100 ps in an x-z plane centered at y = 174.53 nm. Reproduced from Wang [25] with permission from IOP Publishing, copyright 2005.

Thus, to more clearly illustrate this complete solidification procedure, we [26] extended the MD modeling time to 2 ns for the same argon crystal system as above [25]. At 0.5 ns in Figure 9, the liquid region has a higher temperature than the adjacent solid region. Heat transfer between liquid and solid facilitates the cooling of the liquid region to the melting point of argon and even lower. Then solidification starts, and most of the procedure goes under a subcooled condition. The crystallinity function $\phi(r_{i,z})$ defined by Eq. (6) is employed as a criterion to distinguish solid $[\phi(r_{i,z}) > 0.5]$ and liquid $[\phi(r_{i,z}) < 0.5]$. Figure 15 shows the distribution of $\phi(r_{i,z})$ at selected moments of 0.6 ns, 1 ns, 1.5 ns, and 2 ns. It is observed that the liquid region shrinks along with cooling. At 1.5 ns, atomic dislocation (defect) starts to form. $\phi(r_{i,z})$ around 0.5 for the atomic dislocation indicates the severely damaged crystal structure at this location. Although the system and incident energy distribution are symmetric, the defect appears randomly rather than to be symmetric. It may be caused by the asymmetric and nonuniform thermal movement of atoms in the space. Also, the local shear stress in the solid region tends to align the atomic dislocation to the 45° direction relative to the [001] direction of the crystal.

3.2. Dynamic behaviors of stress waves under internal ablation

Above are discussed for surface nano-manufacturing in a free space, where surface atoms can be freely ejected. When the heated region is inside the target, typical internal laser ablation will occur and atom movement is largely constrained by solid surroundings. The internal ablation will

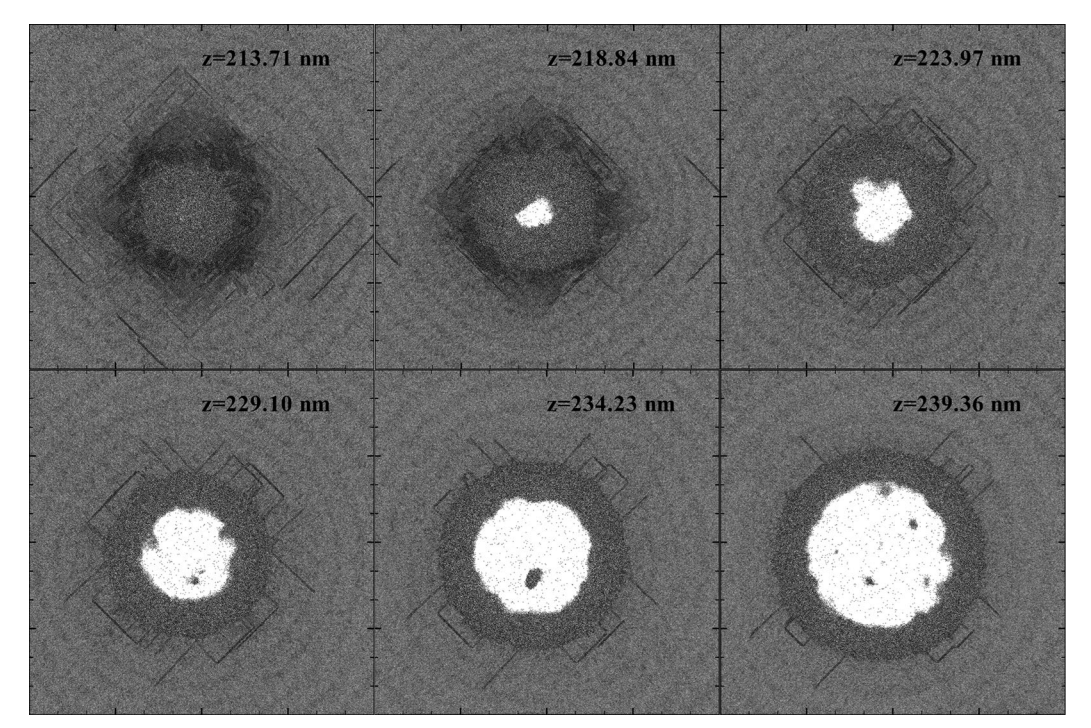


Figure 14. Structural damages in x-y planes at different z locations at 200 ps. z=239.36 nm is the location at the top. Reproduced from Wang [25] with permission from IOP Publishing, copyright 2005.

occur in an extremely high temperature and high-pressure environment. In this case, the atomic behavior is definitely different from that happening in free space. We [27] have studied this process inside an argon target under a pulse heating by using MD modeling, with an emphasis on the phase change status. The target is an argon crystal with dimensions of $108.28\,\mathrm{nm} \times 10.82\,\mathrm{nm}$ \times 108.28 nm (x \times y \times z) and consists of 3,200,000 atoms. The incident laser comes from the top of the target, and is focused at $z = 81.15 \,\mathrm{nm}$ inside the crystal (Figure 16). The heated region has a radius of 2 nm and an absorption depth of 5 nm. The laser pulse energy is 10 J/m² and, to be simplified, the laser intensity is assumed to be uniform over the irradiated area. The laser pulse width is 9 ps. A 1.46 ns simulation duration enables us to uncover stress waves generation and propagation, and stress-induced structure damage in the target.

When the laser pulse is applied to the target, the temperature of the heating region first rises to a high level. A large compressive stress occurs immediately under the combined effect of sharp temperature gradient and thermal expansion of the material. Along with the stress waves propagation, the well-aligned crystal structure is distorted, and damages propagate as well. Figure 16 shows the detailed atom positions at selected moments. At 5 ps, a dark region, caused by damage and atom dislocation, first appears in the directly heated region which exhibits chaotic arrangement of atoms here. It indicates the start of laser ablation and damage generation. In the time span from 5 ps to 100 ps, the target experiences thermal expansion and relaxation. Accompanying the heat conduction, the stress waves stemming from temperature gradient propagates to the boundaries. Note some apparent damages shown in Figure 16 are temporary and will disappear after the stress waves propagate out the region ($t = 40 \,\mathrm{ps}$ in Figure 16). Note the temporary damages here refer to the atomic dislocations caused by the local stresses (both normal and shear stresses) while the stress level does not reach the threshold to cause permanent dislocation. So after the stress waves move out, the atomic dislocations will disappear. Figure 17 shows the evolution of stress distribution in time domain. The dark region in Figure 16 becomes larger along

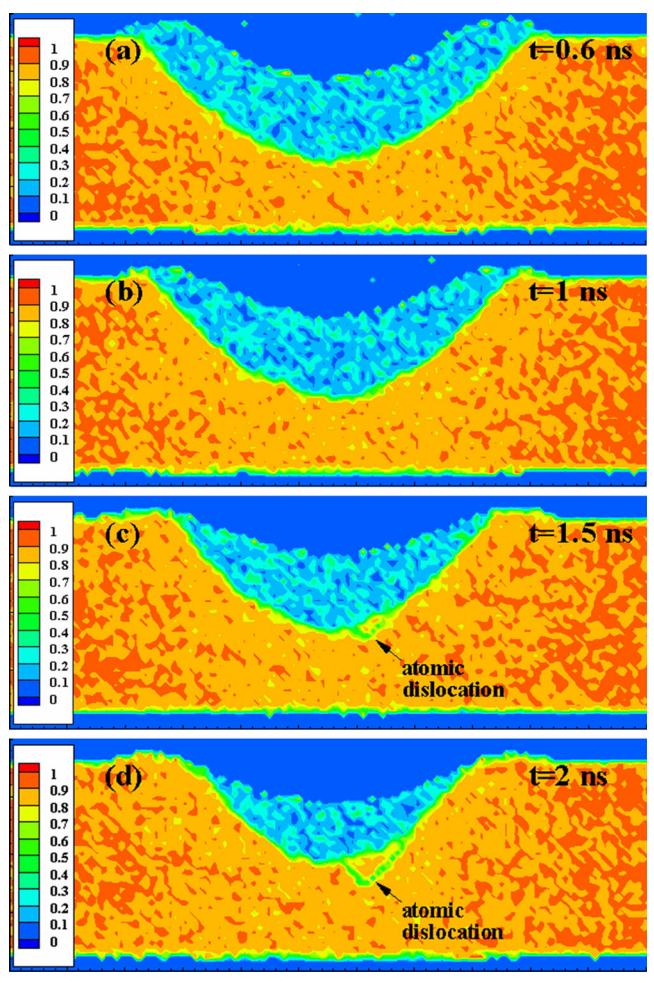


Figure 15. The distribution of $\phi(r_{i,z})$ showing crystallinity at different times in an x-z plane at y=174.53 nm. Reproduced from Wang and Lu [26] with permission from AIP Publishing, copyright 2005.

with the spread of the stress wave. The stress waves are reflected by the periodic boundary in the x direction at around 60 ps, reenters the crystal, and converges at the center again at about 100 ps. After 100s, the stress waves become weaker and the crystal begins recrystallization. The dark region dramatically shrinks, especially around the ablated region, demonstrating the recrystallization of the temporary damages. At the end of modeling, most temporary damages disappear and only the permanent damages are left in the laser heating region (t = 1460 ps in Figure 16).

One thing worth special notice is the thermal equilibrium status during ablation. Figure 18 shows comparison of the velocity distribution of atoms with the Maxwellian-Boltzmann distribution (black line) the selected moments. In the ablation stage, the intense laser heating destroys the thermal equilibrium, making the velocity distribution considerably differ from the Maxwellian-Boltzmann distribution. In this situation, the definition of temperature is less meaningful in the physical sense. After the ablation (50 ps and later), the thermal equilibrium restores and the velocity distribution of atoms again follows the equilibrium Maxwellian-Boltzmann distribution.

Based on the observation of structural evolution, the induced damages can be divided into temporary damages and permanent damages. Comparing the stress distribution and crystallinity distribution inside the target (Figure 19, for the instants of 30 ps, 40 ps, and 60 ps), it is obvious that the local crystallinity significantly decreases when the intense compressive stress wave is

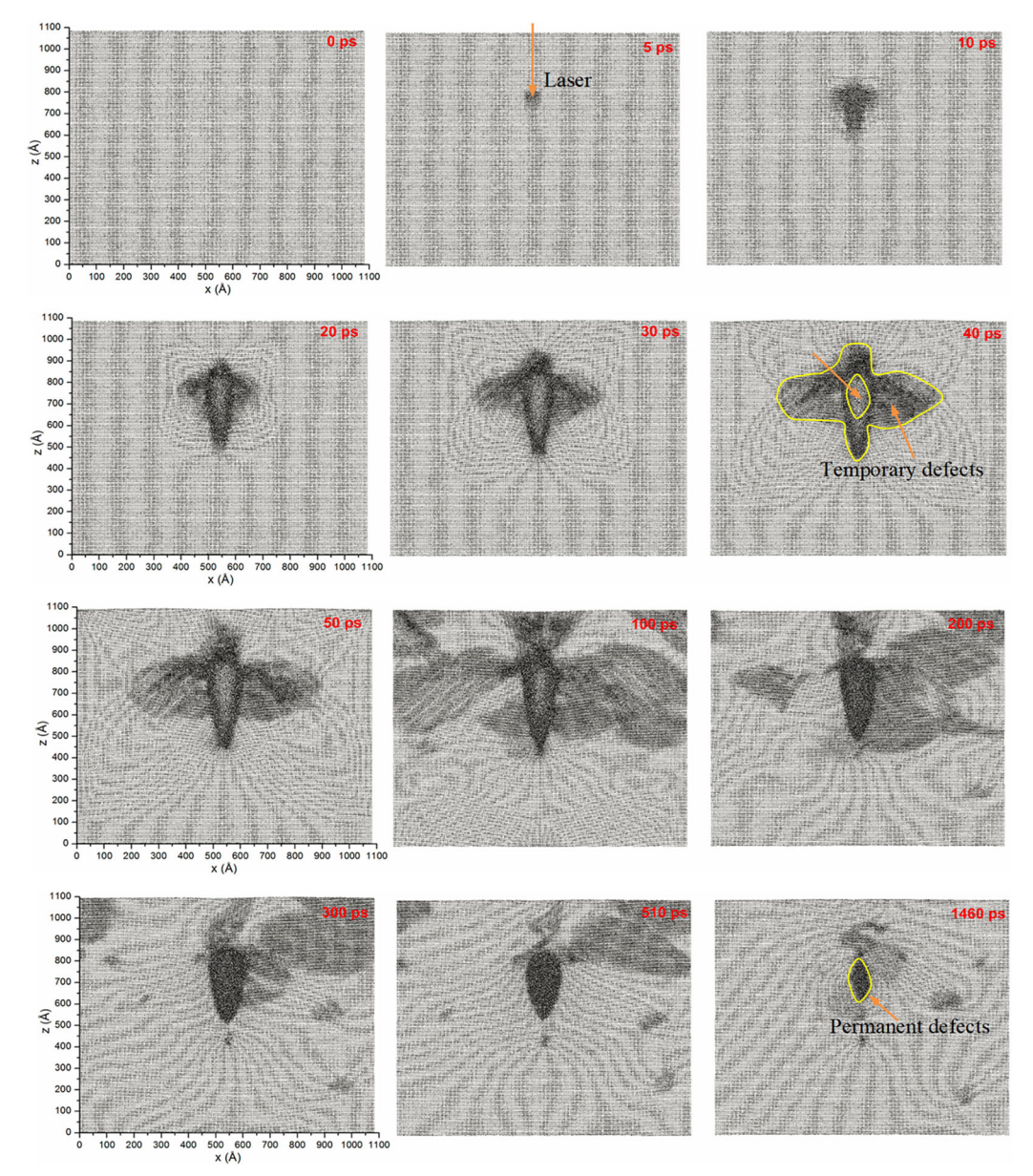


Figure 16. The evolution of atomic positions against time. Reproduced from Li et al. [27] with permission from Taylor & Francis Ltd, copyright 2018.

present. The crystallinity in these regions gradually recovers after the stress waves move out. The permanent damages appear in the ablated region as the local structure experiences the super critical phase change and subsequent solidification. The structure evolution in this region is more complicated and the structure could not recover to the initial crystalline state.

3.3. Stress waves under nano tip confinement

In laser-assisted STM nano-manufacturing, not only ambient gas but also the STM tip confine the shockwaves during laser ablation. Such confinement will affect the recoil pressure in the

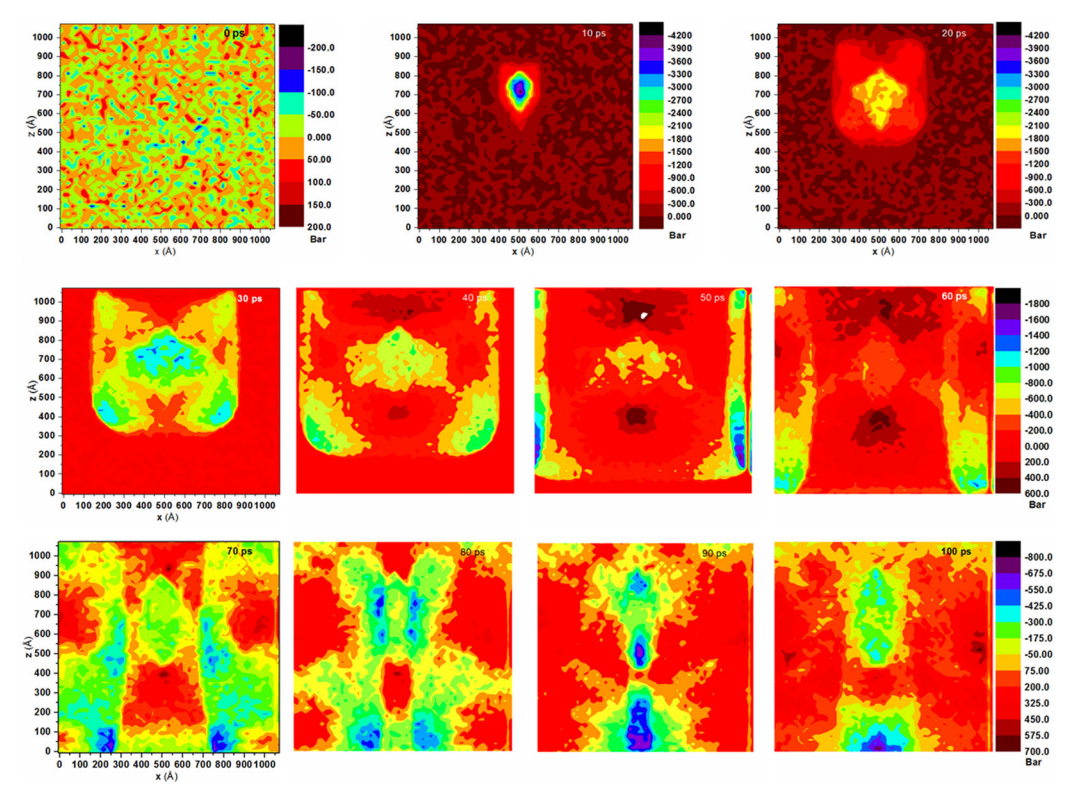


Figure 17. The contour for stress distribution and evolution. Reproduced from Li et al. [27] with permission from Taylor & Francis Ltd, copyright 2018.

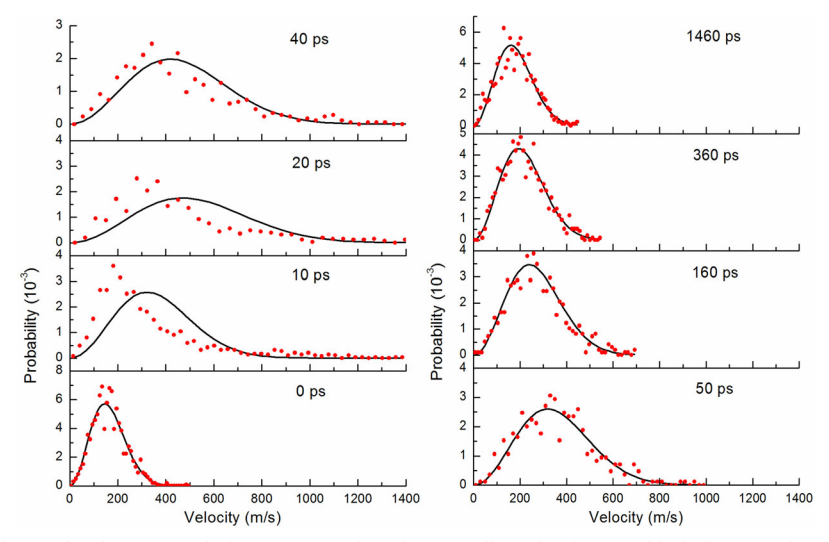


Figure 18. Velocity distributions (red dots) compared with Maxwellian distribution (black line) in the ablated region. Reproduced from Li et al. [27] with permission from Taylor & Francis Ltd, copyright 2018.

target, and affect the stress waves generation. Figure 20 shows our quasi-3D physical model for simulating tip-substrate interaction in the ambient gas under ps laser pulse heating [28]. A conical tip is suspended above an argon crystal substrate. The geometrical parameters of the tip are shown in Figure 20a. The size of the crystalline substrate is $100 \,\mathrm{nm} \times 10 \,\mathrm{nm} \times 30 \,\mathrm{nm} \,(x \times y \times z)$. For the

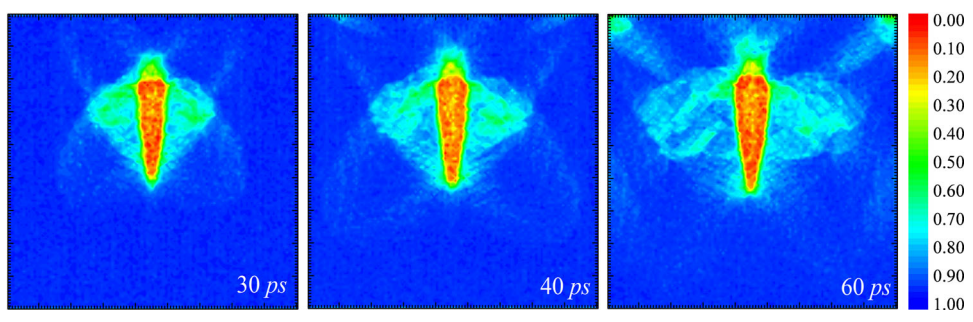


Figure 19. The contour for crystallinity distribution and evolution. Reproduced from Li et al. [27] with permission from Taylor & Francis Ltd, copyright 2018.

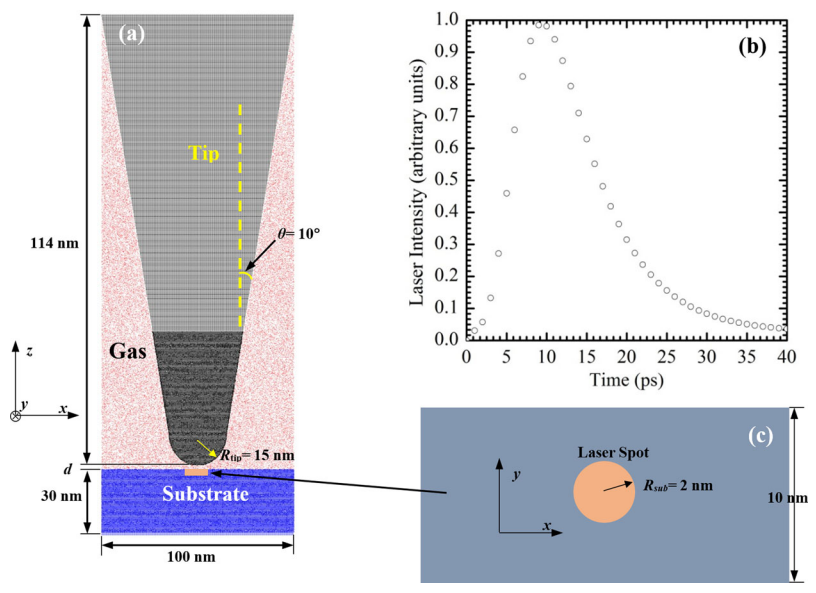


Figure 20. (a) Physical model for simulating the tip-substrate nanostructuring process. (b) Laser beam intensity distribution. (c) Top view of the laser spot. Reproduced from Li et al. [28] with permission from Elsevier, copyright 2016.

physical domain, the periodic boundary condition is applied to both boundaries in the x and y directions, and a fixed boundary condition is applied to the bottom in the z direction. The profile of the laser pulse is shown in Figure 20b. It has a FWHM of 11.5 ps and the peak intensity located at 9 ps. The pulse laser is focused by the tip and results in a spot with 2 nm radius on the top of the crystal. The ambient gas pressure is 0.22 MPa. The initial temperature of this gas-tip-substrate system is 50 K.

By applying a laser pulse energy of $E = 5 \text{ J/m}^2$ with a tip apex-substrate distance d = 2 nm, the temperature contour of the whole physical domain for selected instants is shown in Figure 21. The ablation starts at 10 ps. An obvious hot spot forms with the center temperature higher than 320 K in the substrate beneath the tip apex. From 10 ps to 40 ps, the direct laser-heated region thermally expands and the ablated surface atoms would like to escape upwards. If there is only ambient gas molecules, the ablated atoms will interact with the gas molecules and generate a shockwave in space. However, the existence of the tip above the substrate obstructs the upward ejection of the ablated atoms. They strongly hit the tip apex and then move to the side and form a shock wave around the tip. As these atoms are at high temperatures, the high-temperature front illustrates the shockwave front as shown in the snapshot at 100 ps.

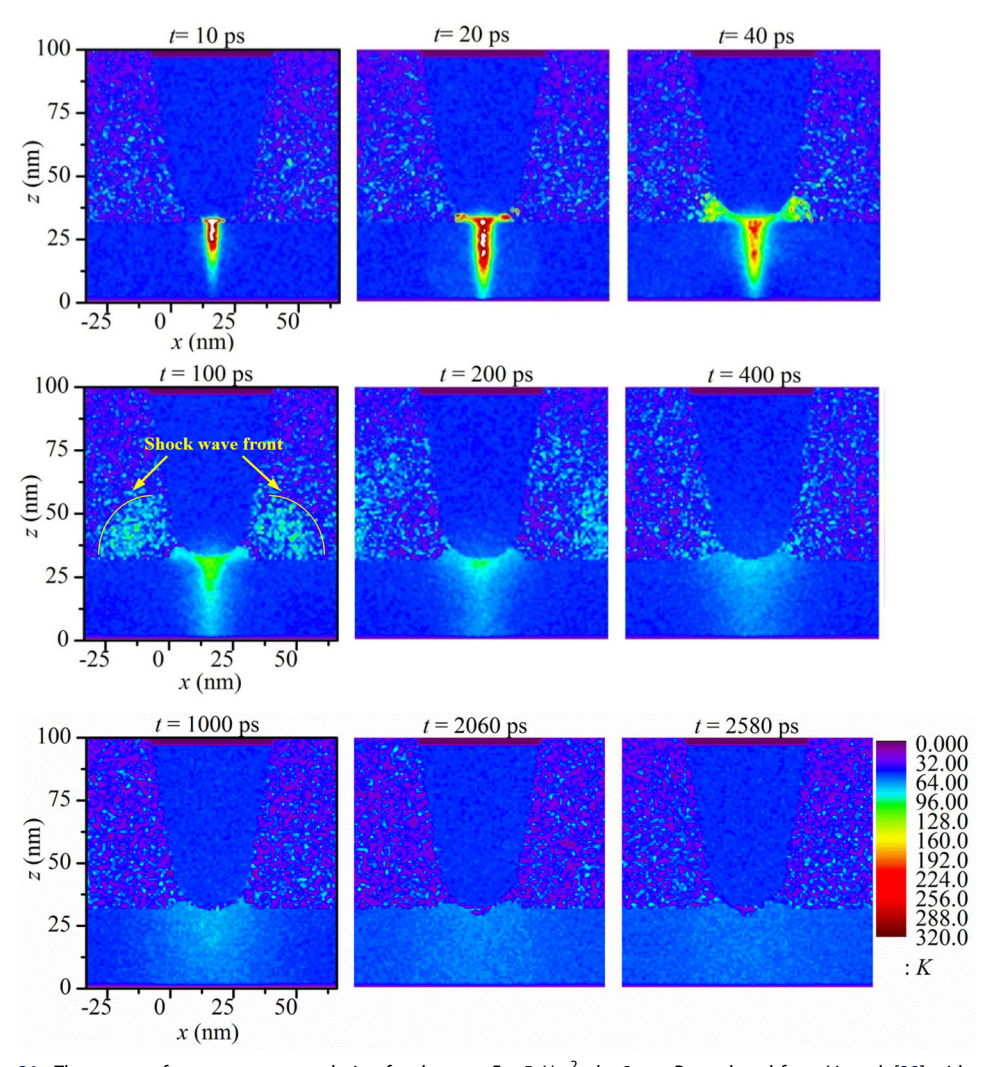


Figure 21. The contour for temperature evolution for the case $E = 5 \text{ J/m}^2$, d = 2 nm. Reproduced from Li et al. [28] with permission from Elsevier, copyright 2016.

In Figure 22, the corresponding crystallinity of the tip and substrate for each instant in Figure 21 is plotted. It is observed that the direct-laser heated region melts when the laser pulse is applied. From 10 ps to 100 ps, the substrate experiences thermal expansion and relaxation. The melted region is enlarged along with heat dissipation. Also, stress waves arise from large temperature gradient and propagates out, causing severe structural distortion around the heated region. From 200 ps to the simulation end (2580 ps), heat transfer continues and the melted region cools down and recrystal-lizes. The stress in the crystal also decreases due to the decreased temperature gradient. Therefore, both the melt region and temporary damage size gradually decrease and disappear at 2580 ps. Some permanent distortion can be still observed at 2580 ps.

Besides the thermal behavior and stress propagation in the substrate, it is interesting to note that, in the tip, the apex crystallinity in the snapshot at 40 ps in Figure 22 is reduced after the strong interaction with the ablated atoms from the substrate. Damages and reshape have been observed at the end of simulation. Laser fluence and tip-substrate distance are two main factors affecting the tip distortion. Figure 23 shows the comparison study of tip distortion under different laser fluences and tip-substrate distances. Doubled laser fluence will result in more severe

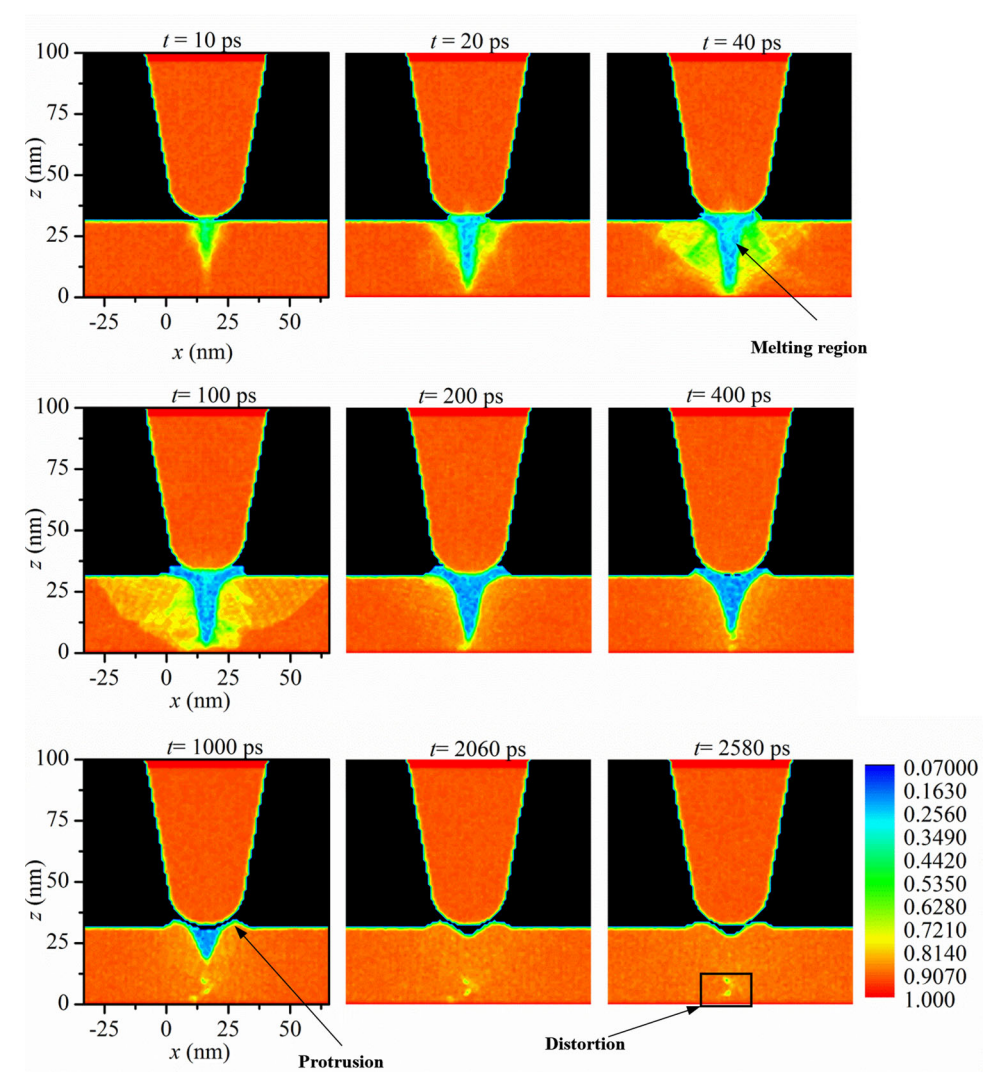


Figure 22. The contour for crystallinity evolution against time of the case E = 5 J/m², d = 2 nm. Reproduced from Li et al. [28] with permission from Elsevier, copyright 2016.

damage in the tip and a blunter apex, as shown in Figure 23a. Figure 23b illustrates that the stronger tip-substrate interaction in the shorter tip-substrate distance will cause a large permanent apex distortion. Also, the tip is found to oscillate due to the interaction with the ablated out plume. During ablation, the surface of the heated region beneath the tip fast expands and explodes upward. The substrate and tip have strong contact immediately afterwards, and then separate. This induces the oscillation in the tip as well as the substrate. The oscillation will be enhanced if the interaction between the tip and substrate increases under higher laser fluence or narrower tip-substrate distance.

4. Experimental nanoscale stress probing

In the above-discussed modeling work, argon is frequently used as the target material due to its well-defined physical properties in a wide temperature range and the simplicity of atomic potential. However, simulation for real applications is hard to achieve because the material properties

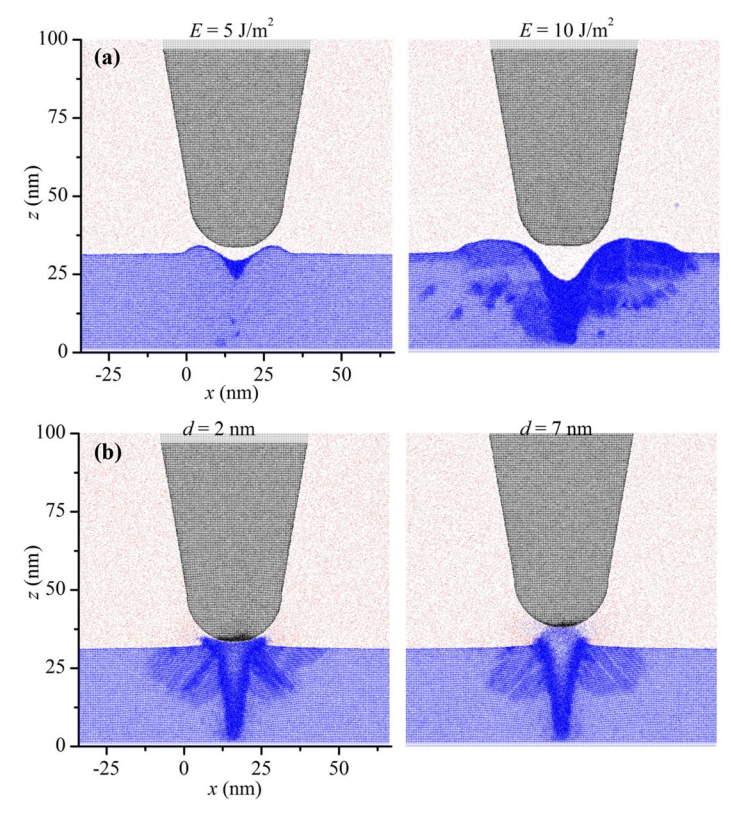


Figure 23. Comparison of tip distortion under different laser fluences and tip-substrate distances (a) Tip profile at $t = 1440 \, \text{ps}$. For both cases, the tip-sample distance is d=2 nm. (b) Tip profile at t=40 ps. For both cases, the laser fluence is 5 J/m^2 . Reproduced from Li et al. [28] with permission from Elsevier, copyright 2016.

may be less understood, ambient condition is very complicated, and the computation is very expensive. Therefore, promising technologies are highly demanded to probe in-situ temperature and stress at the nanoscale. Optical methods, including near-field methods and far-field methods using near-field focusing elements, are featured with non-contact and non-invasion, can access such small scale and measure temperature/stress based on the light-induced physical response. Figure 24 shows a far-field method we have developed [29] which combines Raman spectroscopy and silicon dioxide (SiO₂) micro/nanoparticles. The particle is placed on a silicon (Si) wafer to introduce near-field focusing. When the Raman excitation laser passes through a single particle and is extremely focused to a nanoscale spot on the Si wafer, Raman scatterings from the heated/irradiated area carry fruitful information about the wafer, enabling measurement of local temperature and stress, etc.

The Raman spectrum of Si wafer shows a very strong peak around 521 cm⁻¹. It is the characteristic peak relating to the internal crystalline structure of the wafer. When the temperature of wafer rises, the peak shape will change accordingly. To be specific, the peak intensity will decrease, the FWHM will broaden, and the peak position will shift right (red shift) in the spectrum. These changes are almost linear with temperature rise in a moderate temperature range, thus can be used to measure temperature. Additionally, the peak position of Raman peaks is sensitive to the local stress, while the other two Raman properties are less sensitive. Using this methodology, we measured the Si Raman spectra beneath a SiO₂ nanoparticle (1210 nm diameter) under different incident energies. After taking into account the temperature, stress, and experimental optical system, the local temperature, and thermal stress in the heated area in the Si wafer beneath the single SiO₂ particle are de-conjugated for the first time. The raw information

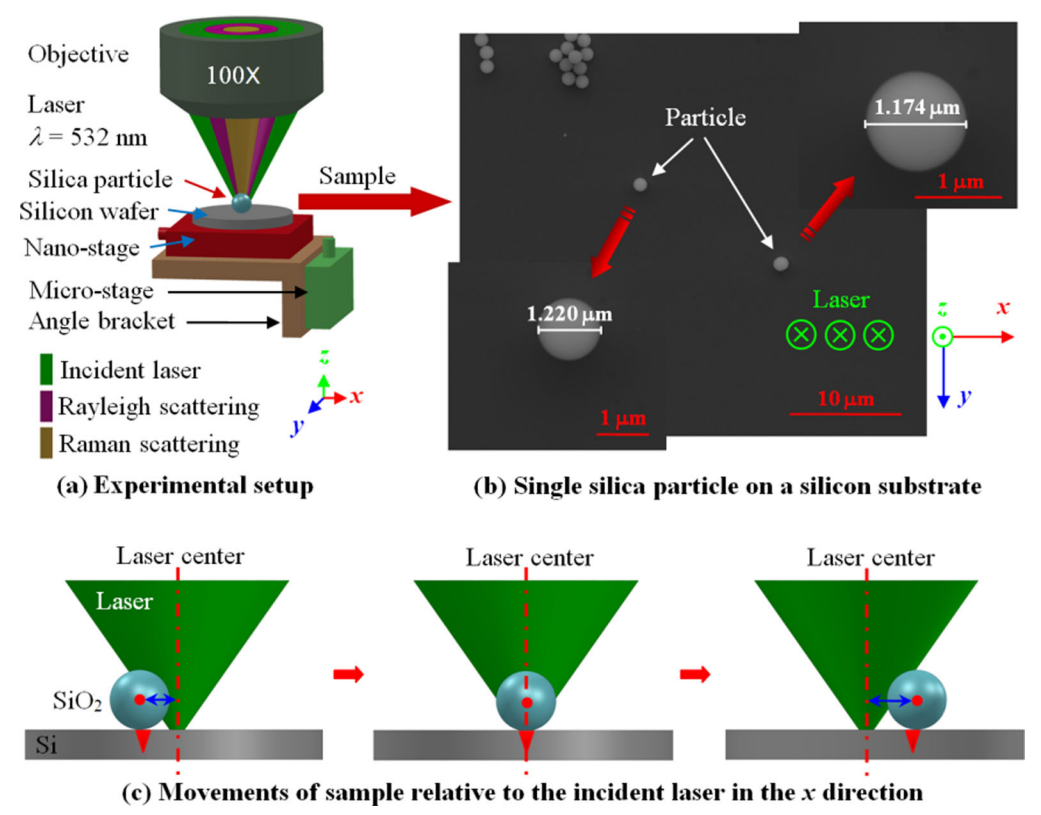


Figure 24. (a) Schematic of experimental setup for near-field thermal and stress probing (not to scale). (b) SEM images of individual nanoparticles on the silicon substrate. Reproduced from Tang et al. [29] with permission from Optical Society of America, copyright 2013.

extracted from the measured Raman spectra is shown in Figure 25a. The subscript "SiO2" denotes the Raman spectra from the Si wafer beneath the nanoparticle, and "Si" denotes the spectra from bare Si wafer. The temperature is first determined based on Raman peak intensity. Since Raman peak intensity is affected by several things besides temperature, the effects from the microscope focusing level, near-field focusing effect, and temperature have been considered. A normalized intensity $\left[I_{\text{SiO}_2}/I_{\text{Si}}\right]/\left[I_{\text{SiO}_2}/I_{\text{Si}}\right]_{E=0}$ is designed to eliminate the non-temperature-related factors. With a calibrated temperature coefficient, the temperature rise is then determined as shown in the first panel of Figure 25b. Out-of-focus effect is ruled out in the temperature determination. However, the out-of-focus effect will bring more significant effect on FWHM and peak position. For FWHM of the Raman peak, it is mainly affected by two factors, temperature and the out-of-focus effect. Thus, the measured change in FWHM is composed of temperature rise-induced change and out-of-focus effect-induced change. With the calibrated FWHM-temperature coefficient from bare Si and the already obtained temperature rise, the out-of-focus effect-induced FWHM change can be obtained (the third panel in Figure 25b). For the shift in peak position, it is a combined result from temperature rise, the out-of-focus effect, and thermal stress. The relation between FWHM and wavenumber shift under out-of-focus condition can be calibrated ahead. Based on the above results, the thermal stress-induced shift can be easily obtained after subtracting the temperature rise-induced one and the out-of-focus effect-induced one, as shown in the bottom panel in Figure 25b.

To pursue physical interpretation of the near-field focusing and heating in the experimental case, modeling and comparison with the experimental result have been conducted in our lab. The nanoparticle focuses the incident laser into a small spot on the Si wafer beneath the particle. The

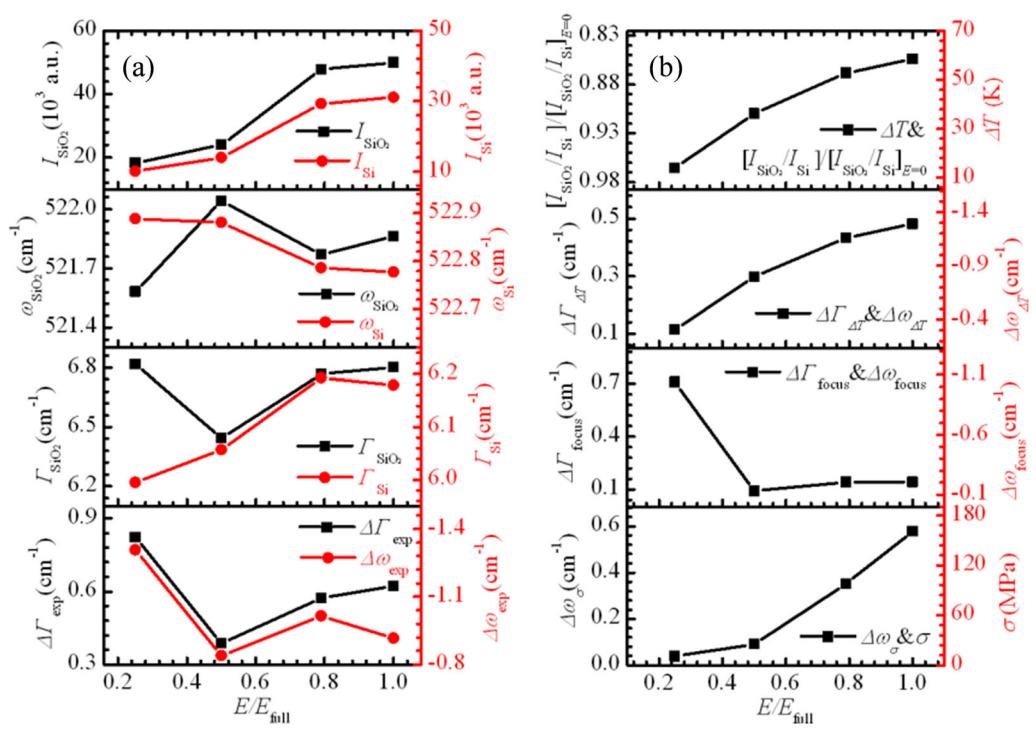


Figure 25. Raman mapping, thermal and stress probing inside silicon under single-particle-focused laser irradiation. Reproduced from Tang et al. [29] with permission from Optical Society of America, copyright 2013.

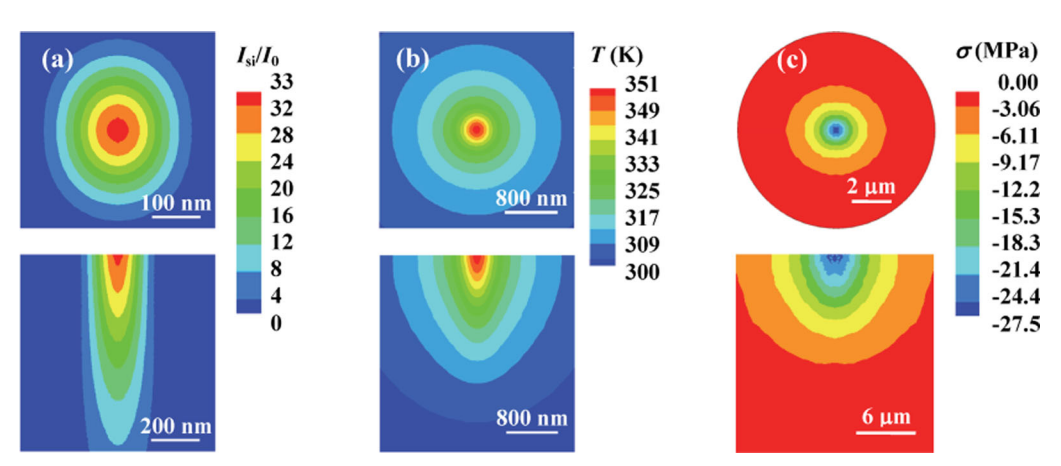


Figure 26. Modeling results for (a) optical, (b) thermal, and (c) stress fields in the Si substrate under near-field optical heating. Reproduced from Tang et al. [29] with permission from Optical Society of America, copyright 2013.

absorbed energy by Si raises temperature and leads to thermal expansion in the wafer. But the region of thermal expansion is confined by solid surroundings, which raises a compressive stress. For the experimental case using the highest incident laser energy, the modeled optical enhancement, thermal, and stress distribution is shown in Figure 26. The modeled temperature rise well agrees with the experimental result, but the modeled stress is much lower. The assumptions for simplifying the model and neglect of minor effects in the experiment may cause this large deviation in stress. A critical factor is the assumed parallel laser beam incidence in modeling that differs from experiment, which is a focused one.

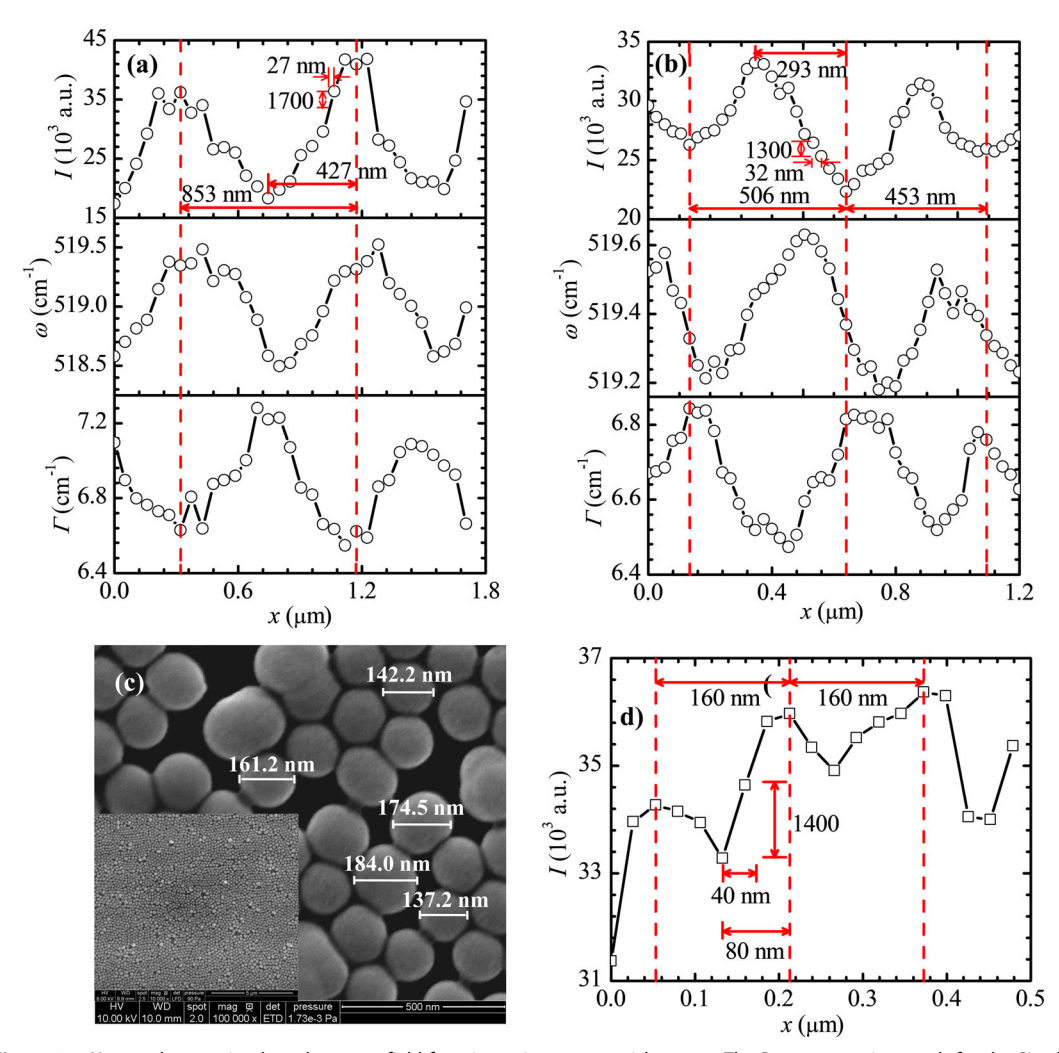


Figure 27. Nanoscale mapping based on near-field focusing using nanoparticle arrays. The Raman scanning result for the Si substrate under particles of (a) 800 nm and (b) 400 nm diameter. (c) SEM images of 160 nm diameter particle arrays on a Si substrate. (d) The Raman intensity of silicon under particles of 160 nm diameter. Reproduced from Tang et al. [31] in accordance with CCO.

By fixing the location of the incident laser, we also probed both temperature and stress measurement in Si beneath nanoparticle arrays under near-field focusing [30]. With scanning over nanoparticle arrays, structure together with temperature, and stress mapping can be realized. Figure 27 shows the nanoscale mapping for near-field heating under 800, 400, and 200 nm particle arrays [30,31]. Raman intensity, FWHM, and peak position vary periodically along with the scanning path, and the length of the period is exactly the same as the particle diameter. This is due to the near-field focusing effect by each individual particle. It was estimated that a scanning resolution of 20 nm can be achieved.

5. Summary and outlooks

Stress waves generation and propagation during laser-material interaction, especially pulsed laser scenario, is a very complicated physical process. It could strongly change the material structure

and affect the phase explosion and subsequent solidification. Understanding of this physical process can take simplified 1D model in both theoretical analysis and MD modeling while modeling under 3D frame can better uncover more physical phenomena not only in thickness direction but also in lateral directions. Temperature evolution, stress waves generation and propagation and the underlying physical mechanisms have been well reviewed and discussed in this work based on our past research. The stress waves are generated from temperature gradient and propagate along with heat transfer. Temporary structure damage/distortion arises when the stress waves are present, but it recovers as the stress waves move out of the region. However, owing to the fast stress waves propagating speed in solid and the slow rate of heat conduction, 3D modeling using MD methods requires a large scale and a long time for the complete simulation from heating, melting, cooling, to solidification. Multi-scale modeling, for instance, combined MD simulation and finite element/difference modeling could help significantly ease computational requirement while still capturing the essential physics [32,33]. For metallic targets, under ultrafast laser heating, the twostep heat transfer model needs to be considered even in MD modeling, which could be achieved by combining MD modeling of atoms and finite difference modeling of electron transport [34]. Simplifications in simulation will raise deviations from experimental results, and simulations alone can only serve as qualitative characterization. Combining simulation and experiment facilitates in-depth understanding of real laser-assisted nano-manufacturing. Still nanoscale temperature and stress probing is extremely challenging, especially for temporal probing. The recent application of a newly observed dual resonance Raman phenomenon provides a very robust and high-sensitivity resonance Raman ratio (R3) method for temperature probing of nanomaterials [35]. Efforts are constantly urged to develop new temperature and stress probing techniques with very high temporal and spatial resolutions.

Acknowledgments

Support of this work by US National Science Foundation (CBET1930866 and CMMI2032464 for. X.W.) and National Natural Science Foundation of China, grant number 52106220 (for S.X.) is gratefully acknowledged.

Disclosure statement

No potential conflict of interest was reported by the author(s).

Funding

This work was supported by Division of Chemical, Bioengineering, Environmental, and Transport Systems, Division of Civil, Mechanical and Manufacturing Innovation, US National Science Foundation (CBET1930866 and CMMI2032464 for. X.W.), and National Natural Science Foundation of China, grant number 52106220 (for S.X.).

References

- C. Wei, et al., "An overview of laser-based multiple metallic material additive manufacturing: from macroto micro-scales," Int. J. Extrem. Manuf., vol. 3, no. 1, pp. 012003, Dec. 2021. DOI: 10.1088/2631-7990/ abce04.
- [2] H. Dobbelstein, et al., "Laser metal deposition of refractory high-entropy alloys for high-throughput synthesis and structure-property characterization," Int. J. Extrem. Manuf., vol. 3, no. 1, pp. 015201, Dec2021. DOI: 10.1088/2631-7990/abcca8.
- P. Nair S, J. Trisno, H. Wang and J. K. W. Yang, "3D printed fiber sockets for plug and play micro-optics," Int. J. Extrem. Manuf., vol. 3, no. 1, pp. 015301, Nov. 2021. DOI: 10.1088/2631-7990/abc674.
- [4] M. S. Dargusch, et al., "Challenges in laser-assisted milling of titanium alloys," Int. J. Extrem. Manuf., vol. 3, no. 1, pp. 015001, Nov. 2021. DOI: 10.1088/2631-7990/abc26b.



- J. Yong, Q. Yang, J. Huo, X. Hou and F. Chen, "Underwater gas self-transportation along femtosecond laser-written open superhydrophobic surface microchannels (<100 µm) for bubble/gas manipulation," Int. J. Extrem. Manuf., vol. 4, no. 1, pp. 015002, Sep. 2022. DOI: 10.1088/2631-7990/ac466f.
- Z. Zhan, et al., "3D printed ultra-fast photothermal responsive shape memory hydrogel for microrobots," [6] Int. J. Extrem. Manuf., vol. 4, no. 1, pp. 015302, Dec. 2022. DOI: 10.1088/2631-7990/ac376b.
- A. Wang, P. Sopeña and D. Grojo, "Burst mode enabled ultrafast laser inscription inside gallium arsenide," Int. J. Extrem. Manuf., vol. 4, no. 4, pp. 045001, Sep. 2022. DOI: 10.1088/2631-7990/ac8fc3.
- [8] F. Caballero-Lucas, K. Obata and K. Sugioka, "Enhanced ablation efficiency for silicon by femtosecond laser microprocessing with Ghz bursts in Mhz bursts (BiBurst)," Int. J. Extrem. Manuf., vol. 4, no. 1, pp. 015103, Jan. 2022. DOI: 10.1088/2631-7990/ac466e.
- [9] X. Wang and X. Xu, "Thermoelastic wave induced by pulsed laser heating," Appl. Phys. A, vol. 73, no. 1, pp. 107-114, Jul. 2001. DOI: 10.1007/s003390000593.
- [10] Z. Ding, et al., "Observation of second sound in graphite over 200 K," Nat. Commun., vol. 13, no. 1, pp. 285, Jan. 2022. DOI: 10.1038/s41467-021-27907-z.
- D. S. Chandrasekharaiah and K. S. Srinath, "Thermoelastic plane waves without energy dissipation in a [11] half-space due to time-dependent heating of the boundary," J. Therm. Stresses, vol. 20, no. 6, pp. 659-676, Sep. 1997. DOI: 10.1080/01495739708956123.
- [12] X. Wang and X. Xu, "Thermoelastic wave in metal induced by ultrafast laser pulses," J. Therm. Stresses, vol. 25, no. 5, pp. 457-473, May 2002. DOI: 10.1080/01495730252890186.
- S. Gacek and X. Wang, "Dynamics evolution of shock waves in laser-material interaction," Appl. Phys. A, vol. 94, no. 3, pp. 675-690, Nov. 2009. DOI: 10.1007/s00339-008-4958-4.
- X. Wang and X. Xu, "Molecular dynamics simulation of heat transfer and phase change during laser mater-[14] ial interaction," J. Heat Trans., vol. 124, no. 2, pp. 265-274, Apr. 2002. DOI: 10.1115/1.1445289.
- [15] S. Xu, H. Zhu, L. Zhang, Y. Yue and X. Wang, "Exploration of physics in laser assisted near-field nanomanufacturing," Chin. J. Lasers, vol. 48, no. 6, pp. 0600001, Mar. 2021. DOI: 10.3788/CJL202148.0600001.
- [16] X. Wang and X. Xu, "Molecular dynamics simulation of thermal and thermomechanical phenomena in picosecond laser material interaction," Int. J. Heat Mass Trans., vol. 46, no. 1, pp. 45-53, Oct. 2003. DOI: 10.1016/S0017-9310(02)00259-4.
- [17] X. Feng and X. Wang, "Nanodomain shock wave in near-field laser-material interaction," Phys. Lett. A, vol. 369, no. 4, pp. 323-327, Sep. 2007. DOI: 10.1016/j.physleta.2007.04.106.
- [18] S. Gacek and X. Wang, "Secondary shock wave in laser-material interaction," J. Appl. Phys., vol. 104, no. 12, pp. 126101, Dec. 2008. DOI: 10.1063/1.3039212.
- [19] S. Gacek and X. Wang, "Plume splitting in pico-second laser-material interaction under the influence of shock wave," Phys. Lett. A, vol. 373, no. 37, pp. 3342-3349, Sep. 2009. DOI: 10.1016/j.physleta.2009.07.044.
- [20] L. Guo and X. Wang, "Effect of molecular weight and density of ambient gas on shock wave in laserinduced surface nanostructuring," J. Phys. D Appl. Phys., vol. 42, no. 1, pp. 015307, Dec. 2009. DOI: 10. 1088/0022-3727/42/1/015307.
- [21] L. Zhang and X. Wang, "Dynamic structure and mass penetration of shock wave in picosecond laser-material interaction," Jpn. J. Appl. Phys., vol. 47, no. 2, pp. 964-968, Feb. 2008. DOI: 10.1143/JJAP.47.964.
- [22] C. Li, J. Zhang and X. Wang, "Phase change and stress waves in picosecond laser-material interaction with shock wave formation," Appl. Phys. A, vol. 112, no. 3, pp. 677–687, Sep. 2013. DOI: 10.1007/s00339-013-7770-8.
- [23] B. Wu, S. Tao and S. Lei, "Numerical modeling of laser shock peening with femtosecond laser pulses and comparisons to experiments," Appl. Surf. Sci., vol. 256, no. 13, pp. 4376-4382, Apr. 2010. DOI: 10.1016/j. apsusc.2010.02.034.
- [24] C. Li, K. Burney, K. Bergler and X. Wang, "Structural evolution of nanoparticles under picosecond stress waves consolidation," Comp. Mater. Sci., vol. 95, pp. 74-83, Aug. 2014. DOI: 10.1016/j.commatsci.2014.07.036.
- [25] X. Wang, "Large-scale molecular dynamics simulation of surface nanostructuring with a laser-assisted scanning tunnelling microscope," J. Phys. D Appl. Phys., vol. 38, no. 11, pp. 1805–1823, May 2005. DOI: 10. 1088/0022-3727/38/11/021.
- X. Wang and Y. Lu, "Solidification and epitaxial regrowth in surface nanostructuring with laser-assisted scan-[26] ning tunneling microscope," J. Appl. Phys., vol. 98, no. 11, pp. 114304, Dec. 2005. DOI: 10.1063/1.2135416.
- [27] Y. Li, C. Li, W. Yao and X. Wang, "Solid-to-super-critical phase change and resulting stress waves during internal laser ablation," J. Therm. Stresses, vol. 41, no. 10-12, pp. 1364-1379, Dec. 2018. DOI: 10.1080/ 01495739.2018.1490634.
- [28] C. Li, L. Zhang, Y. Li and X. Wang, "Material behavior under extreme domain constraint in laser-assisted surface nanostructuring," Phys. Lett. A, vol. 380, no. 5-6, pp. 753-763, Feb. 2016. DOI: 10.1016/j.physleta. 2015.12.001.
- [29] X. Tang, S. Xu and X. Wang, "Thermal probing in single microparticle and microfiber induced near-field laser focusing," Opt. Express, vol. 21, no. 12, pp. 14303-14315, Jun. 2013. DOI: 10.1364/OE.21.014303.



- [30] X. Tang, Y. Yue, X. Chen and X. Wang, "Sub-wavelength temperature probing in near-field laser heating by particles," Opt. Express, vol. 20, no. 13, pp. 14152-14167, Jun. 2012. DOI: 10.1364/OE.20.014152.
- X. Tang, S. Xu and X. Wang, "Nanoscale probing of thermal, stress, and optical fields under near-field laser [31] heating," PLoS One, vol. 8, no. 3, pp. e58030, Mar. 2013. DOI: 10.1371/journal.pone.0058030.
- L. Zhang and X. Wang, "Hybrid atomistic-macroscale modeling of long-time material behavior in nanosec-[32] ond laser-material interaction," presented at International Photonics Optoelectronics Meetings, Wuhan, China, Nov. 1-2, 2012, paper MTh4A.18, 2012. DOI: 10.1364/LTST.2012.MTh4A.18.
- L. Tian and X. Wang, "Pulsed laser-induced rapid surface cooling and amorphization," Jpn. J. Appl. Phys., vol. 47, no. 10, pp. 8113-8119, Oct. 2008. DOI: 10.1143/JJAP.47.8113.
- X. Wang, "Thermal and thermomechanical phenomena in picosecond laser copper interaction," J. Heat [34] Trans., vol. 126, no. 3, pp. 355-364, Jun. 2004. DOI: 10.1115/1.1725092.
- [35] H. Zobeiri, N. Hunter, S. Xu, Y. Xie and X. Wang, "Robust and high-sensitivity thermal probing at the nanoscale based on resonance Raman ratio (R3)," Int. J. Extrem. Manuf., vol. 4, no. 3, pp. 035201, May 2022. DOI: 10.1088/2631-7990/ac6cb1.